FEDERAL UNIVERSITY OF CEARÁ

CENTER OF SCIENCE

DEPARTMENT OF PHYSICS

GRADUATION PROGRAM IN PHYSICS

MASTER DEGREE IN PHYSICS

ERICK JONIHER BOLAÑOS TORRES

ELECTRICAL CHARACTERIZATION OF CELLS WITH CONDUCTIVE ATOMIC FORCE MICROSCOPY

FORTALEZA

2024

ERICK JONIHER BOLAÑOS TORRES

ELECTRICAL CHARACTERIZATION OF CELLS WITH CONDUCTIVE ATOMIC FORCE MICROSCOPY

Thesis submitted to the Graduation Program in Physics of the Center of Science of the Federal University of Ceará, as a partial requirement for obtaining the title of Master in Physics. Concentration Area: Condensed Matter Physics.

Advisor: Prof. Dr. Claudio Lucas Nunes de Oliveira

FORTALEZA

2024

Dados Internacionais de Catalogação na Publicação
Universidade Federal do Ceará
Sistema de Bibliotecas
Gerada automaticamente pelo módulo Catalog, mediante os dados fornecidos pelo(a) autor(a)

B672e Bolãnos Torres, Erick Joniher.
Electrical characterization of cells with Conductive Atomic Force Microscopy / Erick Joniher Bolãnos Torres. – 2024.
57 f. : il. color.

Dissertação (mestrado) – Universidade Federal do Ceará, Centro de Ciências, Programa de Pós-Graduação em Física, Fortaleza, 2024.
Orientação: Prof. Dr. Claudio Lucas Nunes de Oliveira.

1. Conductive AFM. 2. Indium-Tin Oxide. 3. Cell conductivity. 4. Ofcol II. 5. L929. I. Título.
CDD 530

ERICK JONIHER BOLAÑOS TORRES

ELECTRICAL CHARACTERIZATION OF CELLS WITH CONDUCTIVE ATOMIC FORCE MICROSCOPY

Thesis submitted to the Graduation Program in Physics of the Center of Science of the Federal University of Ceará, as a partial requirement for obtaining the title of Master in Physics. Concentration Area: Condensed Matter Physics.

Approved on: 05/08/2024

EXAMINATION BOARD

Prof. Dr. Claudio Lucas Nunes de Oliveira (Advisor)
Federal University of Ceará (UFC)

Prof. Dr. Jeanlex Soares de Sousa
Universidade Federal do Ceará (UFC)

Prof. Dr. Francisco Carlos Carneiro Soares Salomão
Universidade Estuadal do Ceará (UECE)

A mi abuelita Lola. Por sus cuidados y su amor incondicional.

ACKNOWLEDGEMENTS

I would like to express my heartfelt gratitude to my family: my mother Emilce, my father Jorge, my aunts Rocio and Sandra, and my siblings Cristian, Laura, Sergio, Antonia, Estefania, Yael, and Julian, for their unwavering support throughout my life and academic journey. To my partner, Francy, for her support, understanding, and love over the years and for continuing to believe in the process.

A special thanks to Professor Claudio Lucas Nunes de Oliveira for welcoming me into his research group even before my arrival in Brazil, for his trust in me, for his invaluable teachings over the past two years, his patience, and his guidance. And who, in addition to being a great professional, is a great person.

I am grateful to Professor Jeanlex Soares de Sousa for his support and guidance through the experimental challenges and for the trust he has placed in me. I also appreciate his participation in my project defense.

Thanks to Professor Carlos Carneiro Salomão for his advice and assistance with the technical aspects of the experiment, and for participating in my project defense.

My sincere thanks to Dr. Rosemayre Freire for her disposition to assist and guide me with the biological aspects of the work, and for participating in my project defense.

To my colleagues in the Biological Physics Laboratory who have always been ready to offer their help and whom I greatly admire.: Wallace, Joao, Vinnie, Gilvan, Afonso, Brandon, Willian, Alessandro, Damiao, Ednaldo, and Thais.

A special thank you to Isis, who dedicated much of her time to teaching me how to use the microscope, a great professional whom I also admire and respect.

To my friends here in Fortaleza—William, Milena, Michael, Tamia, Alejandra, Yenny, and Evelyn—who have become my family here in Brazil.

To my undergraduate colleagues in Colombia, Hever, Jennifer, and Daniel, who, despite the distance, continue to be present for anything I need.

To my colleague Daniel Brito, for his willingness to discuss ideas about the work. To my classmates Bricio, Cleber, Emanoel, Hertan, Iuri, Yuri, Germano, and Vasco, for their camaraderie in the coursework. This study was financed in part by the Coordenação de Aperfeiçoamento de Pessoal de Nível Superior – Brasil (CAPES) – Finance Code 001, with a scholarship from the Academic Excellence Program (PROEX).

ABSTRACT

Electrical activity plays a vital role in various cellular functions, including signal conduction, muscle contraction, action potentials, and nutrient transport. Investigating these activities poses significant challenges due to the complexity of cellular mechanisms. However, studying the intrinsic electrical properties of cells can provide valuable insights into their state and type, enabling the analysis of variations under pathological conditions and pharmacological treatments. This thesis presents an analysis of the electrical conductivity of cells from two different lineages, OFCOL II and L929, facilitating the study of charge transport mechanisms in different cellular regions and their relation to various biological functions. Conductive Atomic Force Microscopy (C-AFM) was employed to measure the electrical conductivity of these cell lines. The study involved using current distribution images and current-voltage (IV) curves to explore the charge transport mechanism across different cellular regions. Theoretical models were applied to these measurements to gain a deeper understanding of how charge propagates through the cells. AFM provides high-resolution images and quantifies properties such as viscoelasticity and stiffness. Beyond mechanical properties, its variant, C-AFM, has been utilized to measure electrical properties in metals, oxides, semiconductors, and biological samples. To minimize interference, the cells were fixed and cultured on a transparent conductive substrate. This approach enabled detailed and accurate measurements of the electrical properties of the cells, offering new insights into cellular function and behavior.

Keywords: conductive AFM; indium-tin oxide; cell conductivity; Ofcol II; L929.

RESUMO

A atividade elétrica desempenha um papel vital em várias funções celulares, incluindo condução de sinais, contração muscular, potenciais de ação e transporte de nutrientes. Investigar essas atividades apresenta desafios significativos devido à complexidade dos mecanismos celulares. No entanto, estudar as propriedades elétricas intrínsecas das células pode fornecer informações valiosas sobre seu estado e tipo, permitindo a análise de variações sob condições patológicas e tratamentos farmacológicos. Esta tese apresenta uma análise da condutividade elétrica de células de duas linhagens diferentes, OFCOL II e L929, facilitando o estudo dos mecanismos de transporte de carga em diferentes regiões celulares e sua relação com várias funções biológicas. A Microscopia de Força Atômica Condutiva (C-AFM) foi empregada para medir a condutividade elétrica dessas linhagens celulares. O estudo envolveu o uso de imagens de distribuição de corrente e curvas corrente-voltagem (IV) para explorar o mecanismo de transporte de carga em diferentes regiões celulares. Modelos teóricos foram aplicados a essas medições para obter uma compreensão mais profunda de como a carga se propaga através das células. A AFM fornece imagens de alta resolução e quantifica propriedades como viscoelasticidade e rigidez. Além das propriedades mecânicas, sua variante, a C-AFM, tem sido utilizada para medir propriedades elétricas em metais, óxidos, semicondutores e amostras biológicas. Para minimizar interferências, as células foram fixadas e cultivadas em um substrato condutivo transparente. Essa abordagem permitiu medições detalhadas e precisas das propriedades elétricas das células, oferecendo novos insights sobre a função e o comportamento celular.

Keywords: AFM condutivo; óxido de indio-estanho; condutividade celular; Ofcol II; L929.

LIST OF FIGURES

CONTENTS

1 INTRODUCTION

The convergence of diverse subareas within physics, including mechanics, electromagnetism, optics, and statistical mechanics, with biology is a unique perspective and a significant leap in our understanding of biological systems across different scales (Raicu; Popescu, 2008). This multidisciplinary approach, by quantifying observations from macroscopic to microscopic, is instrumental in deciphering the dynamics of the human body and conducting detailed analyses of the physical properties of intricate structures like DNA molecules.

Investigating biological elements at a microscopic level is particularly fascinating as it unveils the foundations of life. The cell, discovered by Robert Hooke in 1665 and recognized as the basic unit of life (Ribatti, 2018), exemplifies a structure of unparalleled complexity, necessitating an interdisciplinary analysis for its complete understanding. Studying the physical properties of cells and the underlying principles governing their processes helps us understand how they interact with their environment, providing insights into their roles in phenomena such as the propagation or prevention of diseases.

Cellular function is significantly mediated by electrical impulses (Hille, 1991). Investigating the charge transport properties within cells offers valuable insights into cellular functional changes that may not be detectable through mechanical studies alone. Given that cells comprise numerous structures and biomolecules, each with specific roles essential for maintaining overall organismal function (Alberts *et al.*, 2008), they can exhibit localized physical property alterations that are not readily apparent using traditional global assessment methods.

Alterations in the electrical properties of cells can be correlated with cardiovascular diseases, mobility disorders, and even cancer (Carvalho, 2021). A detailed understanding of the role of electrical interactions within cells may lead to improved methods for disease detection and prevention, as well as the development of more effective pharmaceuticals.

A major challenge in cellular measurements is achieving precision with minimal interference. Traditional techniques, such as patch clamping and microelectrode arrays, are performed in vivo, leading to substantial interference from the extracellular environment (Hamill *et al.*, 1981). In this study, measurements are conducted directly on the cell with nanometer resolution and picoampere-level current detection, enabling detailed analysis of electrical conductivity across various cellular regions.

Various experimental methodologies are employed to explore the physics of cellular structures. Techniques such as cellular rheology, atomic force microscopy (AFM), and microrhe-

ology provide information about cell morphology and mechanical properties (Haase; Pelling, 2015). Simultaneously, methods like fluorescence microscopy and impedance spectroscopy investigate electrical characteristics (Xu *et al.*, 2016). With the advancement of scanning probe microscopy (SPM), this technique has emerged as an essential tool in studying cells and biomolecules, offering high-resolution images and the ability to quantify properties like viscoelasticity, stiffness, and conductivity (Cheong *et al.*, 2019).

The next chapter comprehensively reviews the techniques used to determine cell electrical properties, encompassing traditional and recent methods. It also reviews processes mediated by electrical interactions in cells. The third chapter details the established methodology for measuring electrical conductivity in two cell lines: OFCOL II (osteoblastic cell) and L929 (fibroblastic cell). Initially, it describes the Conductive Atomic Force Microscopy (C-AFM) technique employed to obtain simultaneous electrical and topographical information from the samples (Suresh, 2007). Following this, it outlines the cell cultivation method using Indium Tin Oxide (ITO) as the substrate and the cell fixation method and provides a description of the experiment and the measurements performed. The fourth chapter presents the results obtained through topographical and current images. These results are subsequently discussed, and an analysis of the IV (current-voltage) curves taken on the cell surfaces is provided. In Chapter 5, concise conclusions from the experimental results are presented.

2 THEORICAL FRAMEWORK

Cells are complex entities composed of numerous subcellular structures and biomolecules, each exhibiting distinct electrical behaviors. For example, nucleic acids and proteins display semiconductor characteristics (Cohen *et al.*, 2005). The plasma membrane functions similarly to a capacitor, or more precisely, as an RC circuit composed of a wide range of linear and nonlinear resistors due to the presence of intrinsic proteins (Hodgkin; Huxley, 1952).

Measuring the electrical properties of cells, particularly those with significant electrical activities like neurons, astrocytes, and fibroblasts, presents a formidable challenge. The electrical signals involved are often below the noise threshold of measurement instruments. Additionally, conducting these measurements in environments closely mimicking in vivo cellular activity is complex. The variety of simultaneous stimuli a cell receives and the presence of electrolytic media that can interfere with measurements further add to this complexity.

Despite these challenges, several measurement methods have been developed to characterize the electrical properties of cells and tissues. In this chapter, we will explore some of these techniques, including Patch Clamp, Electrochemical Impedance Spectroscopy (EIS), and Scanning Probe Microscopy (SPM), with a particular emphasis on Conductive Atomic Force Microscopy (C-AFM). These techniques represent significant advances in understanding the electrical complexities at the cellular and tissue levels.

2.1 Ion Channels and electrical properties of membranes

Ion channels are integral membrane proteins that connect the cytosol and the extracellular medium, allowing the selective passage of specific ions such as Na^+, K^+, Ca^{2+}, and Cl^- across the membrane. This process is passive transport that operates along the electrochemical gradient without requiring an energy source. These channels can transport up to 100 million ions per second, characterized by their high selectivity and gated nature, which can be activated by changes in membrane voltage, ligand binding, or mechanical stress (Alberts *et al.*, 2008).

Non-linear currents over time indicate changes in ionic permeability on the membrane surface, reflecting the presence of specific channels for each ion type. Highly selective Na^+ or K^+ channels controlled by an electric field form voltage-dependent channels, essential for nerve and muscle impulse conduction. Chemically regulated channels, such as the acetylcholine receptor at the neuromuscular junction, respond to neurotransmitter release. Additionally, other

Figure 1 – Schematic of circuit Hodking-Huxley model.

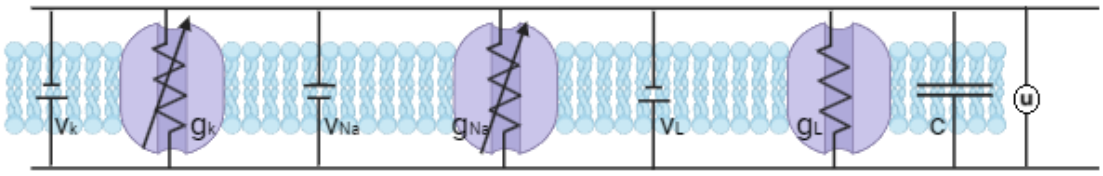

Source: Created by the author.

channels are activated by factors like mechanical stretch, internal Ca^{2+} ions, and agents like cGMP (Keynes, 1985).

The Hodgkin-Huxley model describes the electrical behavior of the membrane by modeling its components as an electrical circuit in parallel, with specific conductances and activation voltages for K^+ and Na^+ channels and an unspecific channel that is the source of a leak current. This model also includes a capacitance (C) and a total voltage (U) across the membrane (Fig. 1). It captures the smooth changes in current through the channels when they open or close and, using a statistical approach, predicts the probability that the channels are open, as described by

$$I = g_{Na}m^3h(U - V_{Na}) + g_K n^4(U - V_K) + g_L(U - V_L). \tag{2.1}$$

The effective conductance of sodium channels is modeled as $g_{Na}m^3h = 1/R_{Na}$, where m describes the activation (opening) of the channel and h its inactivation (blocking). The conductance of potassium is modeled as $g_K n^4 = 1/R_K$, where n describes the activation of the channel, and g_L represents a fixed background leakage conductance (Hille, 1991).

2.2 Excitation-Contraction Coupling in Skeletal Muscle

Excitation-contraction (EC) coupling is the rapid communication between electrical interactions in the plasma membrane and the release of Ca^{2+} from the sarcoplasmic reticulum, transducing an electrical signal into a mechanical response that leads to muscle contraction. The process of EC coupling involves the following sequence:

A potential action is initiated in the plasma membrane of muscle fiber cells by the neurotransmitter acetylcholine, released at the motor end plate by a lower motor neuron, causing membrane depolarization. This action potential then propagates along the T-tubule system. Dihydropyridine receptors (DHPR) detect changes in membrane potential, which are mechanically coupled to ryanodine receptors (RyR) on the sarcoplasmic reticulum. This coupling

triggers the release of Ca^{2+} from the sarcoplasmic reticulum. The concentration of Ca^{2+} in the cytoplasm then increases, allowing Ca^{2+} to bind to the myofilament protein troponin C, ultimately leading to muscle contraction. For muscle relaxation to occur, the concentration of free calcium ions must decline, allowing Ca^{2+} to dissociate from troponin and be recaptured by the sarcoplasmic reticulum (Bers, 2002).

2.3 Traditional techniques

Techniques such as Patch Clamp and electrochemical impedance spectroscopy (EIS), developed in the last century, have been pivotal in studying the electrical activity of individual cells. These methods provide detailed insights into the transport of ions and nutrients between intracellular and extracellular environments, and they help determine dielectric constants, impedances, conductances, and capacitances in biological membranes across various cell types.

2.3.1 Patch Clamp

Developed by Erwin Neher and Bert Sakmann, the *Patch Clamp* technique revolutionized the field of electrophysiology by enabling the measurement of currents in single ion channels (Neher; Sakmann, 1976). This technique is fundamental for studying the electrical activity of individual cells, offering detailed insights into the transport of ions and nutrients between the intracellular and extracellular environments.

The Patch Clamp procedure involves using a glass micropipette containing an electrode and an electrolytic solution. This electrode is connected to an amplifier circuit, a data acquisition system, and a reference electrode placed in the extracellular medium. The microelectrode is immersed in this solution after introducing a saline solution into the micropipette—typically rich in potassium to simulate the cytoplasmic environment. The micropipette is then carefully inserted into the cellular medium. Upon contact with the cell membrane, negative pressure is applied to create a tight seal (a high-resistance seal on the order of Giga-ohms) to prevent unwanted leaks. The micropipettes used in Patch Clamp have tips approximately 1 μm in diameter (Garrill; Davies, 1994). With the seal established, measurements can be performed in configurations such as Cell-attached patch, Whole-cell patch, Inside-out patch, and Outside-out patch, as illustrated in Fig. 2.

The Whole-cell patch configuration has been widely used to monitor neuronal

Figure 2 – Patch Clamp Technique

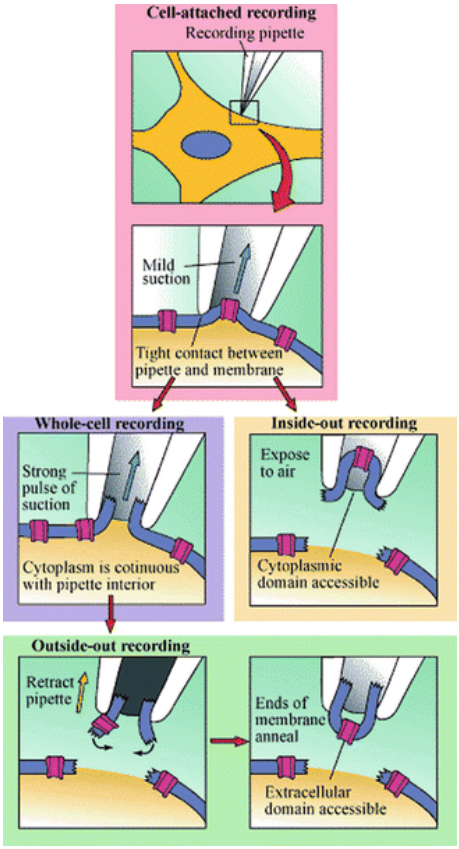

Source: (Yan; Wu, 2013).

activity in vivo across various species, particularly in rats, allowing the observation of changes in membrane potentials under different sensory stimuli. Recordings can be made from pre- and post-synaptic regions and other cellular locations (Petersen, 2017). Additionally, Patch Clamp has been applied to investigate other types of cellular activities, such as the study of calcium channels in embryonic kidney cells (Armstrong *et al.*, 2010) and the analysis of ion transport across fungal membranes, identifying different types of channels (Garrill; Davies, 1994).

Quantitative analyses are conducted by modeling an equivalent circuit from which relevant equations are derived. A simplified example is shown in Fig. 3, representing a circuit formed by the micropipette, the seal at the tip, and the membrane. Here, V_p is the potential in the pipette, and V_m, R_m, and C_m are, respectively, the potential, resistance, and capacitance of the membrane, with R_a representing the resistance between the membrane and the pipette, and I the current through the membrane.

It is important to note that the circuit in Fig. 3 is a simplification. In practice, Patch Clamp includes an amplification system to record measurements. When focusing on the conductance of a specific ion, such as K^+, additional variables must be considered, including the voltage at each ion channel and its linear or nonlinear nature (Wilson *et al.*, 2011). The technique

Figure 3 – Equivalent Circuit for Whole-Cell Patch

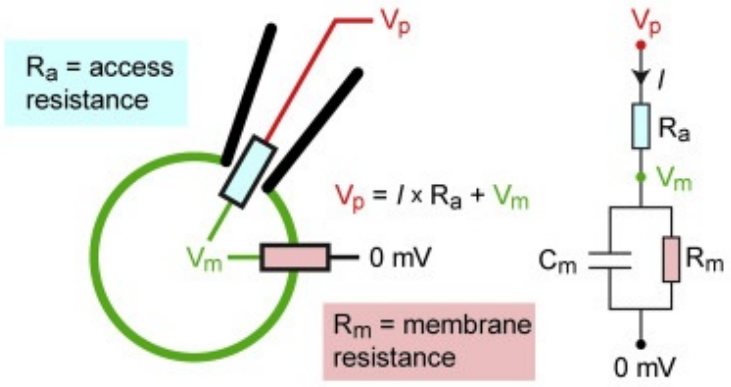

Source: Adapted from (Petersen, 2017).

also presents limitations, such as difficulty in maintaining a constant signal, the limited number of ion channels that can be studied, and the extensive data recording time.

Despite its limitations, Patch Clamp remains an indispensable technique for research in cellular physiology and neuroscience, offering a resolution of millivolts and milliampere currents and allowing for the detailed study of the electrical properties of cell membranes.

2.3.2 Electrochemical impedance spectroscopy

Electrochemical Impedance Spectroscopy (EIS) is an essential technique for investigating electrical properties in electrochemical systems such as batteries, electrochemical sensors, corrosion phenomena, and biological systems like living cells. The principle of EIS is based on measuring impedance and capacitance by perturbing the system in a steady state with a sinusoidal voltage or current signal and analyzing the response at the same frequency. This technique allows the characterization of electrical properties as a function of frequency.

In the EIS configuration, an electrochemical cell comprises a working electrode (WE), a reference electrode (RE), and a counter electrode (CE), all connected to a potentiostat and immersed in an electrolyte solution. The WE is the site of the reactions of interest, while the RE, with a known and stable potential, allows precise measurement of the WE's potential. The CE completes the circuit. Similar to Patch Clamp, the analysis involves modeling an equivalent circuit.

During the analysis, a small amplitude oscillatory voltage, $V(t)$, is applied between the reference and working electrodes. The resistance in the electrolyte medium, R_u, arises from the current movement between the electrodes. The charging and discharging at the electrode-

Figure 4 – Schematic of EIS.

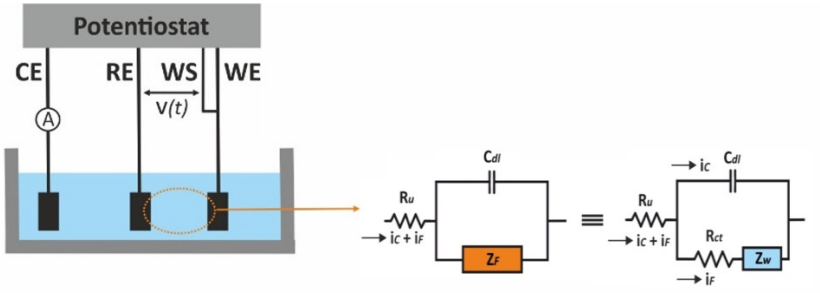

Source: Adapted from (Lazanas; Prodromidis, 2023).

electrolyte double layer (WE) is a capacitance, C_{dl}. Additionally, the faradaic current i_f with general impedance Z_f is considered, as illustrated in Fig. 3. The WS refers to the working sense lead, added to enhance the voltage measurement accuracy.

The current through R_u is divided between the capacitance current i_c and i_f, the latter resulting from the kinetics of redox reactions and the diffusion of redox species toward the working electrode surface. Therefore, Z_f is described by

$$Z_f = R_{ct} + Z_w, \tag{2.2}$$

where R_{ct} is the charge transfer resistance and Z_w is the Warburg impedance, a generalized impedance (Lazanas; Prodromidis, 2023).

In general, the impedance Z in an RC circuit is a complex number, where the real component corresponds to the electrical resistance R, and the imaginary part is the capacitive reactance χ,

$$Z = Z_{Re} + Z_{im}, \tag{2.3}$$

$$Z = R - i\chi, \tag{2.4}$$

where $\chi = \frac{1}{\omega C}$, with ω being the signal frequency and C the capacitance.

Applications of EIS to characterize the electrical properties of cells and tissues date back to the 1920s and 1930s, with studies by K. S. Cole and H. Frick determining dielectric constants, impedances, conductances, and capacitances in biological membranes of blood cells (Cole, 2020). The general relaxation theory was subsequently applied to study the electrical properties of cell suspensions and biomolecules, analyzing dielectric behavior over a broad frequency spectrum (Schwan, 1957). In the 1970s, Takashima demonstrated that the capacitance of the squid giant axon membrane varies with depolarization and hyperpolarization (Takashima, 1976).

Figure 5 – Electrode Configurations for Impedance Measurements.

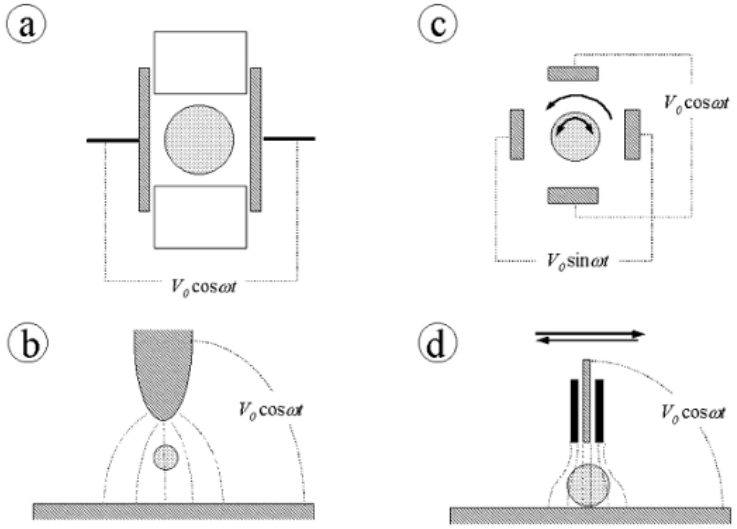

Source: (Asami, 2002).

Recent technological advances have enabled the fabrication of devices to study impedance in individual cells (Han *et al.*, 2002). In subsequent studies using this device for different stages of breast cancer, it was shown that the electrical resistance in breast cells decreases as the cancer becomes more aggressive while the phase of the impedance increases (Han *et al.*, 2007).

There are different configurations for impedance characterization. The standard configuration is the traditional parallel plate capacitor electrodes, which is more reliable for giant cells (Fig. 5a). For smaller cells, techniques such as dielectrophoresis and electrorotation are more suitable (Fig. 5b and 5c, respectively). An approach that allows for a more detailed scan of dielectric properties over the cell surface is the scanning dielectric microscope, which uses a fine probe as the electrode to scan the region of interest (Fig. 5d).

Despite the widespread use of EIS to characterize electrical properties in cells and tissues, the drawback is that the impedance of the extracellular fluid often masks the impedance values of the cell. Recently, the coplanar electrode configuration has been widely adopted because it simplifies fabrication and minimizes the effect of extracellular fluid impedance by keeping the cell in contact with the electrodes (Fig. 6).

An equivalent circuit scheme introduces a correction factor that eliminates the effect of extracellular impedance. Here, R_s is the extracellular fluid resistance, C_s is the extracellular fluid capacitance, I_s is the extracellular fluid current, R_c is the cell resistance, C_c is the cell capacitance, I_c is the cell current, R_e is the electrode resistance, and I_2 is the total system current.

Figure 6 – Coplanar Electrode Configuration.

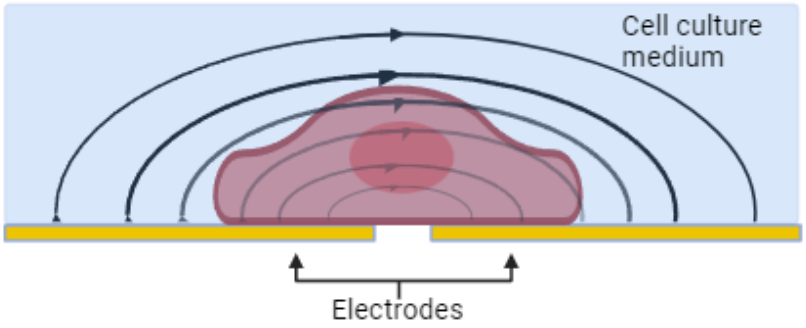

Source: Author.

The coplanar electrode configuration has evolved into what is known as a multi-electrode array, which not only measures the impedance of cells and tissues but also allows for high-definition impedance imaging (Bounik *et al.*, 2022). However, the manufacturing complexity and the relatively low signal-to-noise ratio make it a technique that requires further precision for the detailed characterization of cell electrical properties.

2.4 Electrical measurement in cells with Scanning Probe Microscopy

Scanning probe microscopy (SPM) has emerged as a powerful tool for studying the electrical properties of biological materials under various conditions. Specifically, atomic force microscopy (AFM) in its electrical modes, such as Conductive AFM (C-AFM), Kelvin Probe Force Microscopy (KPFM), and Electrostatic Force Microscopy (EFM), allows for the measurement of distinct properties of samples, including conductivity, electrostatic forces, and surface potential. These techniques also provide detailed information about the sample's surface charge distribution and topography.

C-AFM has been instrumental in studying various biological samples' conductive and electronic transfer properties. For example, analyzing conductance in proteins and DNA has advanced the understanding of charge transport mechanisms in these molecules. Conductivity is analyzed under various configurations and environments, revealing that transport depends on the orientation and context of the measurement (Shinwari *et al.*, 2010). C-AFM studies also include investigating electronic transport in substances like neuromelanin and ferritin in the human substantia nigra, showing quantum behaviors similar to those of quantum dots (Rourk, 2019).

Conductivity measurements in specific cells, such as hippocampal neurons, PC12 cells, and astrocytes, have been carried out using C-AFM (Zhao *et al.*, 2020). These cells,

Figure 7 – Equivalent Circuit for Coplanar Electrodes.

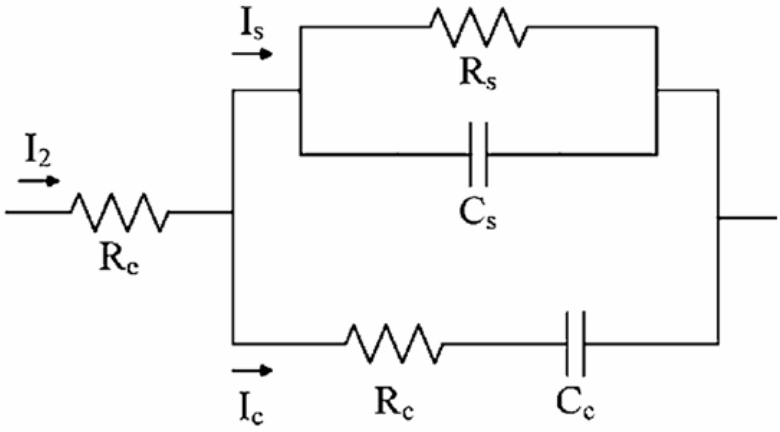

Source: (Tsai *et al.*, 2014).

cultured on gold substrates and air-dried, exhibited capacitive characteristics in the cell body, while the dendrites of PC12 cells behaved like metallic nanowires.

Comparative research between healthy and cancerous breast cells revealed that both types exhibit capacitive characteristics in the cell bodies. However, the dendrites of cancerous cells demonstrated semiconductor behavior, in contrast to the capacitive behavior observed in healthy cells (Zhao *et al.*, 2022).

KPFM and EFM have been utilized to electrically study biological samples' surfaces under static and dynamic conditions. Cell communication, ion and nutrient exchange, and mobility can be understood by studying the physical properties of cell surfaces. The study of contact potential difference (CPD) in air-fixed astrocytes showed that the cell body has a CPD approximately 2.7 times larger than the glial filaments.

Microbial adhesion on medically relevant surfaces like stainless steel and gold has also been studied using KPFM. The CPD of methicillin-resistant Staphylococcus aureus USA100 (MRSA) cultured on these substrates showed changes in potential after incubation on each surface. This suggests that the type of substrate may affect cellular metabolism, and consequently, its propagation will depend on the substrate on which it is cultured (Birkenhauer; Neethirajan, 2014). Changes in the CPD of PC12 cells after being treated with various stimulants were detected using KPFM. The CPD on the surface of PC12 cell membranes is not homogeneous and is primarily negative before treatment. After treatment with reactive oxygen species (ROS), dopamine, and zinc ions, the CPD shifted positively (Tsai *et al.*, 2012).

Using EFM, it was determined that the surface charge density on the membrane of

neurons ranges from -8.4x10^4 C/m^2 to 3x10^5 C/m^2, before and after injecting charge on the surface (Zhao *et al.*, 2019). The mobile charge density in the pili of *Geobacter sulfurreducens*, along with the dependence of charge density on temperature and pH, was similar to that of carbon nanotubes. This finding suggests that the pili of *G. sulfurreducens* function as molecular wires with delocalized charge transport, rather than the hopping mechanism typical of biological electron transport (Malvankar *et al.*, 2014).

2.5 Atomic Force Microscopy (AFM) and Conductive Atomic Force Microscopy (C-AFM).

2.5.1 AFM

Atomic Force Microscopy (AFM), an advanced technique within the category of Scanning Probe Microscopy (SPM), operates through an ultrafine tip, generally with an apex radius smaller than 40 nm, mounted at the end of a support known as a cantilever. The interaction between the tip and the sample results in the cantilever deflection obeying Hooke's Law

$$F = -k \cdot \delta, \tag{2.5}$$

where δ represents the deflection and k is the spring constant (Oliveira *et al.*, 2012).

The cantilever deflection is detected by a laser system at its top surface, reflecting onto the center of a photodiode divided into four quadrants. During the lateral scanning of the tip over the sample surface, the processing unit converts the laser displacement on the photodiode into topographical data. Movements of the sample or tip along the X, Y, and Z axes are controlled by piezoelectric scanners, providing a resolution of up to 1 nm in the XY plane and 0.1 nm along the Z axis (Lanza, 2017, ch. 1).

2.5.1.1 Working modes of AFM

AFM operates in several modes, each designed for specific applications and types of measurements. These modes of operation work in different ranges of the tip-sample distance, as shown in Fig. 8. For each mode, there is a different tip-sample interaction force, as follows,

- Contact Mode: This mode keeps the tip in the repulsive region of the graph, with a very small distance between it and the sample.
- Intermittent Contact Mode (Tapping Mode): The tip oscillates between the contact and the negative potential regions.

Figure 8 – Operating Modes of AFM

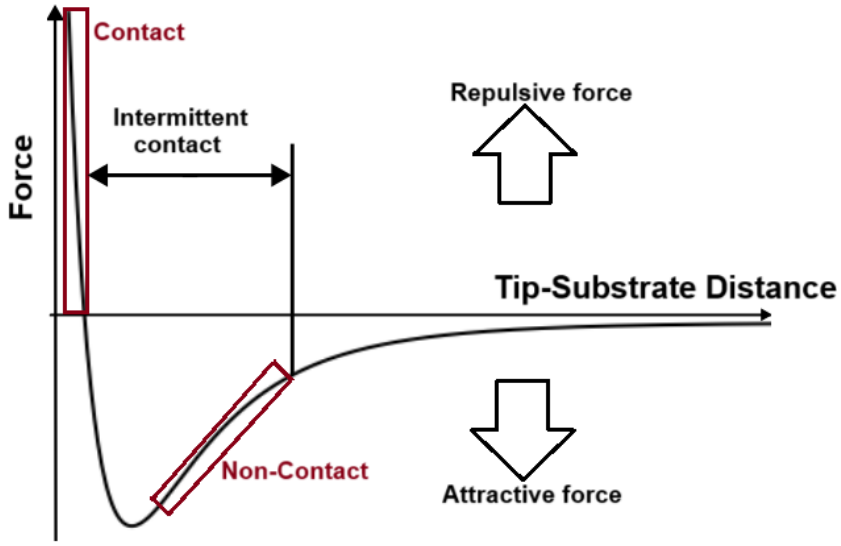

Source: Created by author.

- Non-Contact Mode: The tip vibrates above the sample in the attractive region.

2.5.1.2 Contact Mode

The contact mode, also known as constant force mode, scans the sample while applying a preselected and configured constant force. This mode is frequently used to obtain high-definition images of complex samples. It is also used for imaging soft matter but with a shallow set point and scan speed.

The equipment maintains a constant force by not varying the cantilever's deflection, whose spring constant is known beforehand. The scanning is performed in the X and Y axes, while the Z-axis uses a feedback loop that adjusts the voltage in the Z piezoelectric element to keep the cantilever deflection constant.

While contact mode can achieve exact topography measurements, it has the disadvantage of causing significant wear on the tip. In the case of electrical measurements, the tip may lose its conductive coating.

2.5.2 Conductive AFM (C-AFM)

Conductive Atomic Force Microscopy (C-AFM) configuration is similar to that of standard AFM, with the critical difference being that the tip must be conductive. An amplifier circuit is also required to measure the current flowing through the junction between the tip and the sample, as shown in Fig. 9. The amplifier circuit captures the current, converts it from analog

Figure 9 – Schematic of C-AFM

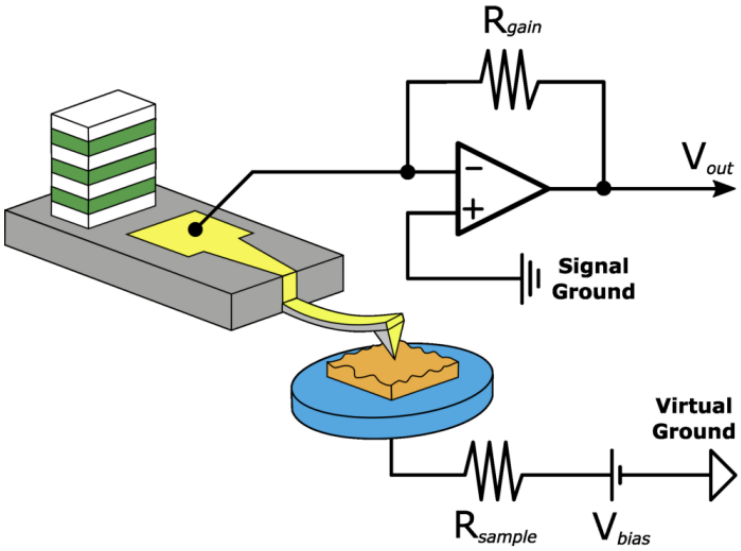

Source: MFP-3D User Guide, Chapter: Conductive AFM (ORCA) Hardware.

to digital, and processes it through the software.

The C-AFM technique provides detailed topographic images of the sample and enables current spectroscopy. Measurements are performed by placing the sample on a highly conductive substrate connected to the operational amplifier's ground. A potential difference is applied, and upon making contact with the sample, the conductive tip closes the circuit, allowing the measurement of the current passing through the nano-junction.

3 MATERIALS AND METHODS

3.1 Procedures

This work focuses on measuring the electrical conductivity in two cell lines using Conductive Atomic Force Microscopy (C-AFM) in an air environment. This method aims to avoid interference in current readings due to reactions at the interface between the cantilever and the culture medium, which is typically an ionic solution.

3.1.1 Confocal Fluorescence Microscopy

The cells were fixed with paraformaldehyde, permeabilized with Triton X-100, and blocked with BSA. F-actin filaments were stained with phalloidin, and cell nuclei were stained with 4',6-diamidino-2-phenylindole dihydrochloride (DAPI) (100 ng/ml in PBS). Confocal microscopy images were obtained at room temperature using a Zeiss LSM 710 laser scanning confocal microscopy system (Zeiss, Jena, Germany), with excitation at 405 nm and 488 nm, and maximum emission at 457 nm and 518 nm for nuclei and F-actin, respectively.

3.1.2 Atomic Force Microscope

For C-AFM measurements, the MFP-3D-BIO microscope, integrated with an inverted microscope and manufactured by Asylum Research (Digital Instruments, Santa Barbara, CA), was used. In ORCA mode (Optimized Resistance Conductance Amplifier), this equipment is specialized for C-AFM operations in contact mode. The standard configuration of the MFP-3D includes a cantilever holder equipped with a bias wire Fig. 10a). Additionally, the sample holder features a non-conductive plate with gold-coated magnets at each end. Electrical contact is established by a wire extending from one of the magnets to a clip that secures the substrate to the base of the plate Fig. 10b). The complete setup is formed by connecting these two parts through the biasing wire, which is attracted to the magnet, as demonstrated in Fig. 10c).

3.1.3 Conductive Probe

The probes used in the experiment are the model NanoWorld® Arrow™ CONTPt made from monolithic silicon, which is highly doped to dissipate static charge. These probes feature a rectangular AFM cantilever with a triangular free end and a tetrahedral AFM tip with a

Figure 10 – Experimental setup of the standard ORCA. (a) Standard ORCA cantilever holder connected to the polarization wire. (b) Sample holder for ORCA mode. (c) Standard ORCA setup on the AFM.

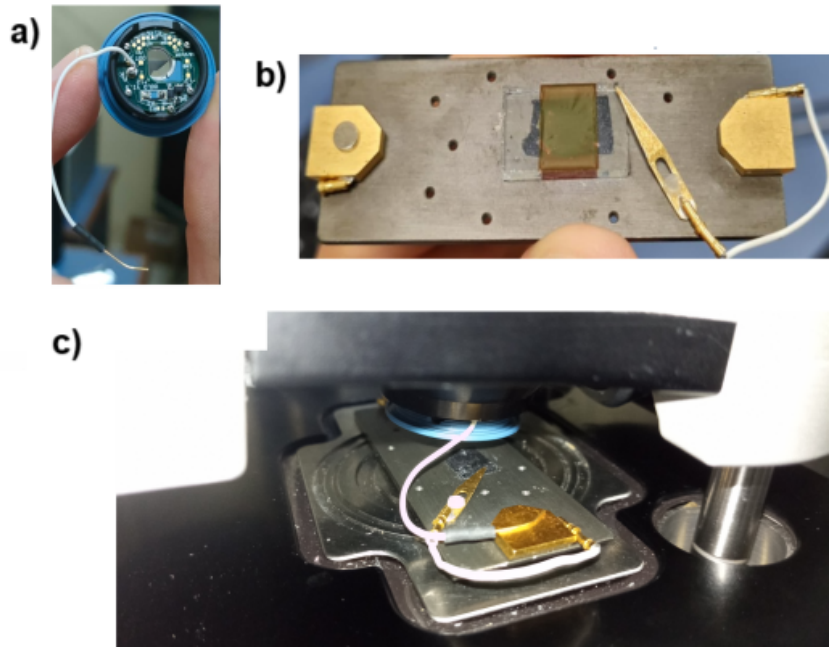

Source: Created by the author.

typical height of 10 - 15 μm. Fully coated with a 23 nm thick platinum iridium5 (PtIr5) layer deposited on both sides of the cantilever, the tip radius of curvature is less than 25 nm. The nominal spring constant of the probes is measured at $k = 0.2$ N/m, and they have a resonance frequency of $f = 14$ kHz. The PtIr5 coating makes the probes suitable for C-AFM measurements, while the low spring constant is ideal for working with delicate biological samples such as cells.

This configuration ensures the precision and sensitivity required for cell C-AFM measurements, enabling detailed analysis of the electrical properties of the biological samples under study.

3.1.4 Conductive substrate ITO

Indium Tin Oxide (ITO) is a conductive and transparent film widely used in research related to solar cells. In this study, cell culturing is performed on ITO substrates chosen for their exceptional electrical and optical properties, including low resistivity (<10 x 10^{-4} Ω cm) and high transparency (>90%) (Chen *et al.*, 2013). Previous studies have successfully cultured cells on ITO, such as in (Moon *et al.*, 2020), where it was used to investigate the viability and adhesion of cardiomyocytes under electrical stimulation and for imaging conductivity through currents generated by redox reactions stimulated at the ITO- culture medium interface using a

laser (Wu *et al.*, 2019).

3.1.5 ITO treated with poly-L-lysine (PLL)

The surface of the ITO was initially cleaned with deionized water and subsequently sterilized in an autoclave. It was then coated for 15 minutes with a 0.01% Poly-L-Lysine solution (Sigma-Aldrich) and washed with sterile PBS.

3.1.6 Cell Culture

On an ITO-coated slide previously treated with PLL, thoroughly cleaned, and sterilized, cells are cultured at a density of 125,000 cells/cm^2 for 24 hours following the protocol described in (Sousa *et al.*, 2020). Briefly, cells are cultured in Dulbecco's Modified Eagle Medium (DMEM) with high glucose concentration, supplemented with 10% fetal bovine serum and 1% penicillin-streptomycin, maintained at 37° in a 5% CO_2 atmosphere.

3.1.7 Cell Fixation

To perform the measurements without interference from the ionic medium and to preserve the cellular structure as intact as possible, the cells were fixed with paraformaldehyde following this protocol: After 24 hours of cell culture, the cells were removed from the culture room. The medium was then removed, and the cells were rinsed with PBS three times, each lasting 5 minutes. Subsequently, the cells were immersed in 4% paraformaldehyde for 15 minutes, followed by two more rinses with PBS. Finally, the cells were rinsed twice with deionized water to remove excess PBS. After fixation, the cells were air-dried. Once dry, a conductive magnet was attached to the substrate, and the samples were taken to the AFM for measurement.

3.1.8 OFCOL II Cells

The OFCOL II cell line originates from mouse bone marrow and is of the osteoblast type (Oliveira *et al.*, 2008). Osteoblasts are bone matrix cells originating from mesenchymal stem cells (MSCs) (Pittenger *et al.*, 1999). The function of osteoblasts is to form new bone and contribute to the growth of existing bone tissue.

Figure 11 – Alternative experimental setup that allows monitoring of cells with the inverted microscope of the MFP-3D BIO.

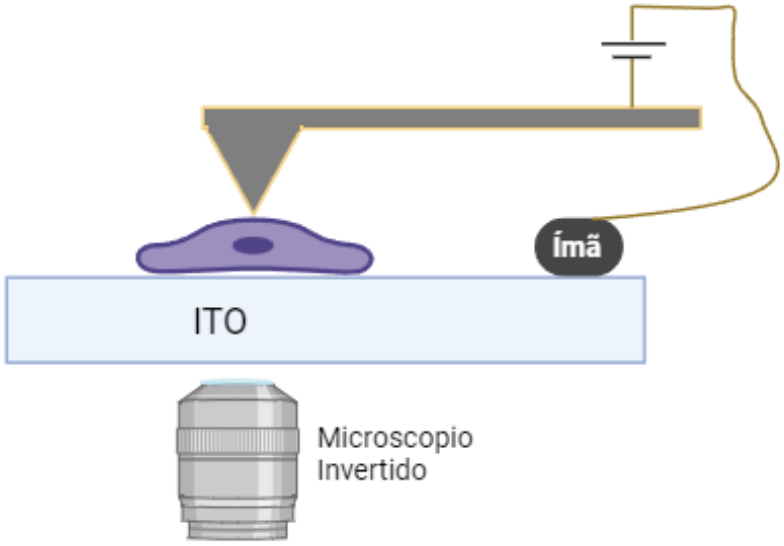

Source: Created by the author.

3.1.9 L929 Cells

L-929 cells are a fibroblast cell line derived from the subcutaneous connective tissue of a 100-day-old male C3H/An mouse. Fibroblasts provide a stromal structure to various tissues and play a crucial role in wound healing, being the most common cells in connective tissue. They are a dynamic cell type, with functions that include synthesizing structural elements such as collagen, tissue repair and renewal, and body protection against infections and injuries (Phipps *et al.*, 1997).

3.1.10 Experimental Setup

The inverted optical microscope integrated with the MFP-3D is crucial for locating regions of cellular interest. Therefore, the standard ORCA setup could be better for our experiment. After applying the cell fixation protocol, the end of the ITO substrate is cleaned, and a conductive magnet is attached with silver glue. Fig. 11 proposes an alternative setup that allows for the direct observation of cells with the inverted microscope, connecting the polarization wire to the magnet previously fixed on the ITO.

3.1.11 Measurement Protocols

The measurements were carried out in two stages. The first stage involved scanning the sample of interest, and the second stage involved performing current-voltage curves at the topographically interested points.

Before starting the measurements on the cells, the cantilever's spring constant was calculated using the thermal noise method included in the Igor software. Subsequently, the conductive properties of the ITO were measured by performing IV curves on the sterilized substrate treated with PLL. This also verified that the apex of the tip allowed the passage of current. Once this was done, the sample was placed in the AFM. A scan was performed to avoid damaging the sample by applying a force of 5.6 nN and a voltage of 5 V to the sample. The scan was carried out at a frequency of 0.2 Hz, allowing for the recording of current flow through the cells.

Once the topography and current image are obtained, three points on the cell are selected from three different regions at varying heights. At these points, a current-voltage (IV) curve is acquired using a ramp with an amplitude of 10 V at a frequency of 0.1 Hz.

4 RESULTS AND DISCUSSIONS

4.1 ITO Characterization

Cells were cultured on a glass slide coated with Indium Tin Oxide (ITO). The slide's dimensions are 1.1 mm in height, 5 cm in length, and 2.5 cm in width. The thickness of the glass layer is 1800 ± 205 Å, with an etching time of less than 240 seconds and a sheet resistivity of less than 10 Ω/sq.

Figure 12a shows the topography obtained with AFM on the substrate, where it can be observed that the surface of the ITO is uniform and rough, with a root mean square

Figure 12 – Electrical and Surface Evaluation of ITO Treated with Poly-L-Lysine. a) Topography of the ITO substrate covered with PLL. b) I-V curve obtained on the PLL coated ITO substrate

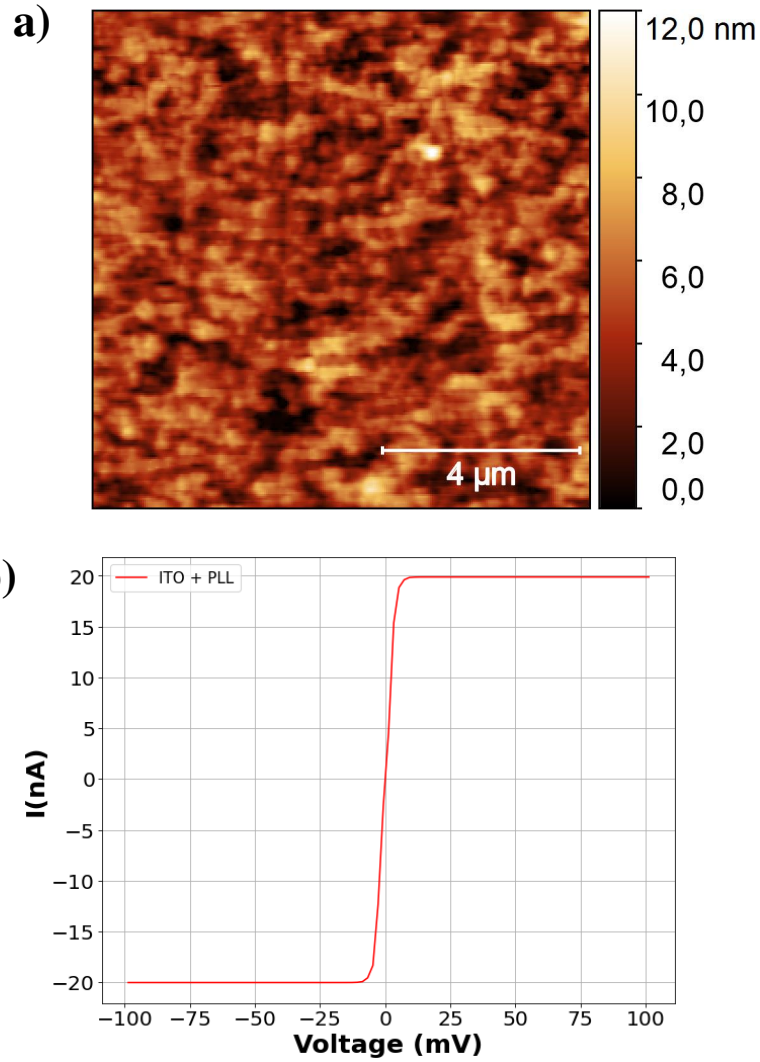

Source: Created by the author.

(RMS) roughness of 1.696 ± 0.259 nm. Compared to the size of the cell, this is considered low roughness. A conductivity test was also performed on the ITO surface of the ITO treated with Poly-L-Lysine. For this purpose, C-AFM was used to measure IV curves at various points on the ITO surface (Fig. 12b), which demonstrated Ohmic behavior with an electrical resistance of a few hundred kilo-Ohms, consistent with reported values in (Paiman *et al.*, 2020).

The irregularity of the ITO surface enhances cell adhesion to the substrate. Furthermore, its low electrical resistance makes it an ideal substrate for electrical conductivity measurements. The high transmittance of ITO also allows for seamless integration with the MFP-3D BIO microscope.

4.2 Morphology of L929 and OFCOL II Cells by Fluorescence Microscopy

First, the morphology of the cell lines was studied using fluorescence microscopy to gain insights into the cell interior. This technique allowed us to visualize the distribution of actin filaments, which are part of the cytoskeleton and the cell nucleus.

Actin filaments, also known as microfilaments, are primarily composed of two helically intertwined polymer chains of actin with a diameter of approximately 7 nm. These microfilaments are cytoskeleton components located just beneath the plasma membrane, playing a crucial role in maintaining cell shape. Additionally, they are involved in muscle contraction, cell adhesion and motility, intracellular transport, and cytokinesis (Cooper, 2000). The nucleus is a membrane-bound organelle found in eukaryotic cells and contains most of the cell's genetic material. Its primary function is to regulate gene expression and mediate DNA replication during the cell cycle (Lodish *et al.*, 2008). The size of the nucleus is correlated with cell size; it is the largest organelle and occupies approximately 10% of the cell's volume (Alberts *et al.*, 2008).

The fluorescence images of L929 and OFCOL II cells are presented in Figs. 13a and 13b, respectively. Actin filaments, highlighted in green, exhibit an elongated and well-distributed morphology across the cell surface in both cell types, with increased concentration towards the extremities. Visualized in blue, the nucleus is centrally located within the cell body. L929 cells display smaller extremities and a predominantly flattened nuclear region, whereas OFCOL II cells exhibit elongated extremities and a significantly rounded nuclear region. These fluorescence imaging results confirmed that L929 and OFCOL II cells remained viable and structurally intact following the fixation protocol, indicating their suitability for subsequent conductivity experiments.

Figure 13 – The morphology of cells imaged by fluorescence microscopy a) Image of the L929 cell. b) Image of the OFCOL II cell.

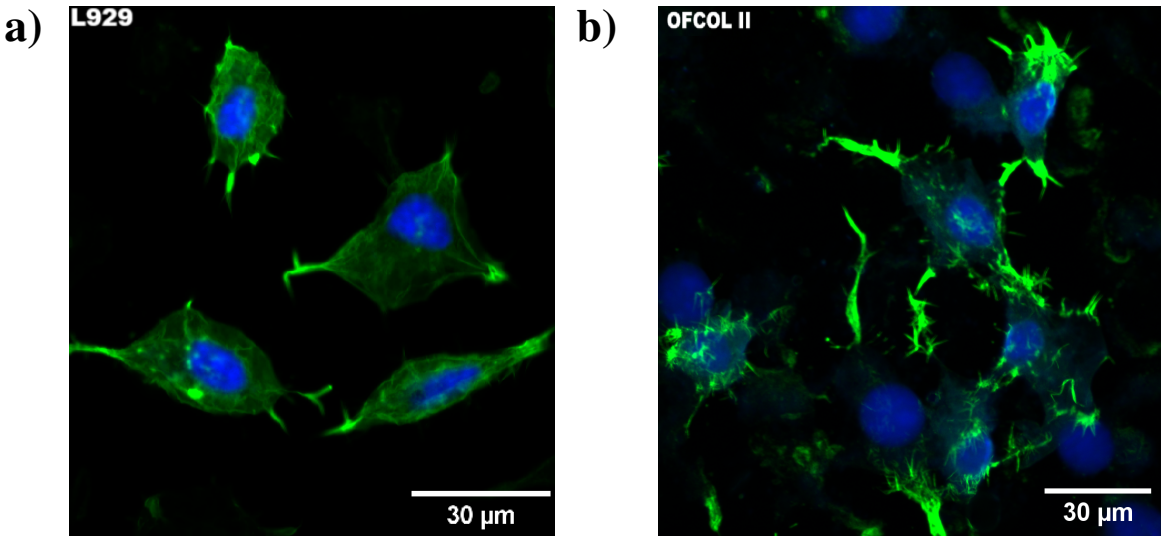

Source: Created by the author.

4.3 Electrical Conductivity in L929 Cells Investigated by C-AFM

A specific region on the plate with the cells was selected using the inverted microscope integrated into the MFP-3D BIO, leveraging the high transmittance of the ITO. This selection ensured a consistent distance between the cells and the contact point of the magnet with the polarization wire, minimizing variation across different cells. A topography and current image were acquired using C-AFM on the L929 cells, as shown in Figs. 14a and 14b. The applied force was set at 5.6 nN, and the scanning frequency was 0.2 Hz. At this force and frequency, efficient electrical contact between the AFM tip and the cell was maintained without causing damage to the sample. It is well-documented that images taken with 10 nN or higher forces can damage biological samples (El-Naggar *et al.*, 2010). Moreover, the indentation produced by the tip is minimal compared to the overall cell size, which is on the order of several hundred nanometers. All topography and current spectroscopy images were processed using Gwyddion software version 2.65 (Nečas; Klapetek, 2012).

In the topography image of the L929 cell, a distinct protruding region over the main cellular body can be identified. Comparison with the fluorescence microscopy images reveals that this elevated section corresponds to the nuclear region, as indicated by the green rectangle in Fig. 14a. The area highlighted in blue corresponds to the region with the highest density of actin filaments, representing the cell's lower-height section. Figure 14b displays the current image across the cell when a potential difference of 5 volts is applied between the tip and the sample.

By correlating this with the topography image, it can be inferred that the current flow through the nuclear region is more significant than in other regions of the cellular body.

Figure 14 – Electrical conductivity in L929 cells investigated by C-AFM a) Topography image of the L929 cell. b) Image of the L929 cell c) Current and Height profile of line red in a).

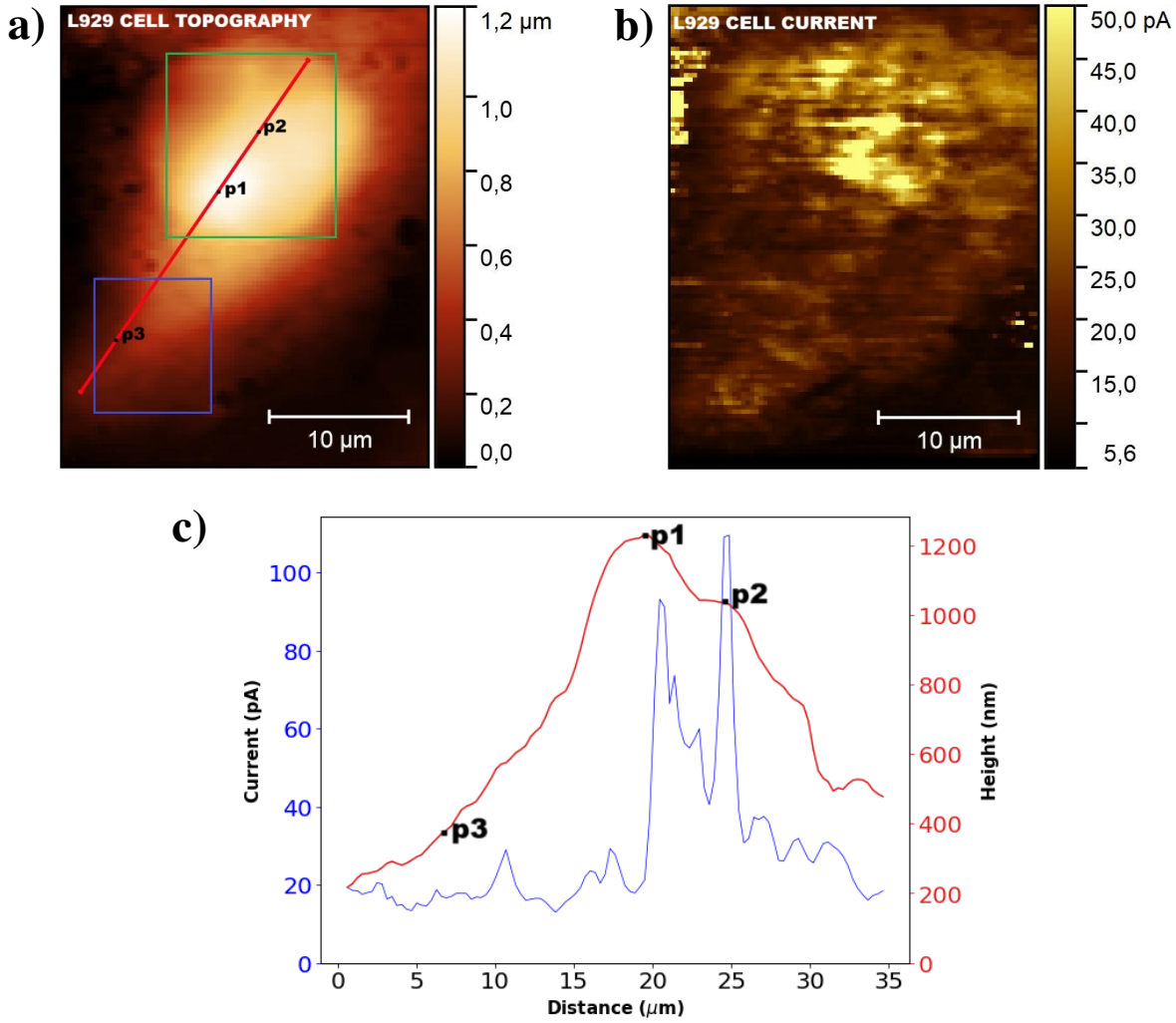

Source: Created by the author.

The dimensions of the cells were measured, with the length defined as the distance between the farthest extremities, the width as the greatest distance perpendicular to the length, and the height as the maximum distance from the substrate. The average length of the cells was 34.56 $\pm$ 1.31 μm (N=12), and the width was 23.5 $\pm$ 0.87 μm (N=12). These measurements align with previously reported values (Ma *et al.*, 2023), indicating that the size of L929 cells typically ranges from 20 to 50 micrometers. The mean cell height was determined to be 894.35 $\pm$ 57 nm (N=12).

In the nuclear region of the cell, two distinct areas can be identified: a higher, rounded

Figure 15 – Current distribution in: a) the nuclear region and b) the extremity of the L929 cell body.

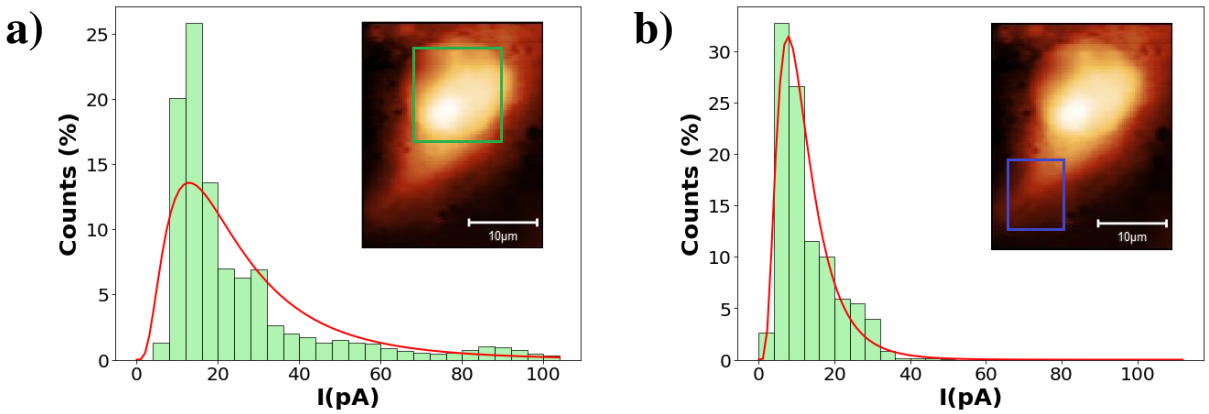

Source: Created by the author.

area and a lower, flatter area, marked as points 1 and 2 in Fig. 14a. Figure 14c presents the height and current profiles traced along the red line in Fig. 14a, demonstrating that point 1 corresponds to the highest elevation in the cell. In contrast, point 2 represents an intermediate elevation located within the nuclear region. Point 3, positioned at one of the cell's extremities, lies outside the nuclear region and exhibits a lower height. The current profile (blue line) in Fig. 14c increases in the areas of greater height according to the cell's height profile (red line). The predominantly round shape of the highest area suggests the presence of the nucleolus; corroborating findings reported in (Pederson, 2011).

One significant advantage of Conductive Atomic Force Microscopy (C-AFM) is its ability to study electrical conductivity in specific regions of a sample. Figures 15a and 15b present the current distribution in the nuclear region and the extremity of the cell body, respectively. The average current value in the nuclear region was 28.7 $\pm$ 5.71 pA (N=12), while in the cell extremity, it was 16.98 $\pm$ 1.78 pA (N=12). This variation can be attributed to the nuclear region's high concentration of biomolecules, such as DNA, which has been extensively investigated for its electrical conductivity (Shinwari *et al.*, 2010). Furthermore, histone proteins within the nucleus may also contribute to charge transport through the cell. In contrast, the extranuclear regions are primarily composed of the cytoskeleton and the plasma membrane, the latter being well-known for its low electrical conductivity (Saulis, 2010).

Current-voltage (I-V) curves were obtained at points 1, 2, and 3, as illustrated in Fig. 17. The waveform was a linear ramp at a rate of 4 volts per second, with an amplitude of 10 volts and a frequency of 0.1 Hz, as shown in Fig 16. The general behavior observed in the forward sweep (from -10 to 10 V) and the reverse sweep (from 10 to -10 V) suggests a

linear dependence of current on voltage and a small hysteresis, possibly due to charge storage effects between the sample and the tip. Consequently, the I-V curve analysis for the L929 cells was approximated using a model of an ohmic material connected in parallel with a constant capacitance capacitor.

We employ the following procedure to assess the repeatability and determine if the behavior of the IV curve changes with repeated measurements at the exact location: For each designated point, IV curves were recorded in four segments, with each segment comprising four curves. The segments were separated by 5, 10, and 20 seconds without removing the tip from the cell surface. No significant trend or change in the behavior of the IV curves was observed with the increasing number of measurements taken at the same point.

For the calculations, the average of the four curves from each segment was taken, and the average of each segment was linearly fitted, as shown in Fig. 17. In the statistical analysis, only the IV curves with a linear fit having an $R^2 > 0.97$ were considered. The graphs shown in Fig. 18 are consistent with the current spectroscopy image, where the nuclear region exhibited higher conductivity compared to the extremity of the cell body. The mean electrical resistance of the nucleolus (p1) was 79.64 GΩ, slightly higher than that of the rest of the nucleus (p2), which was 73.74 GΩ. Additionally, the extremity showed a considerably higher resistance, with an

Figure 16 – AC voltage applied to the cell.

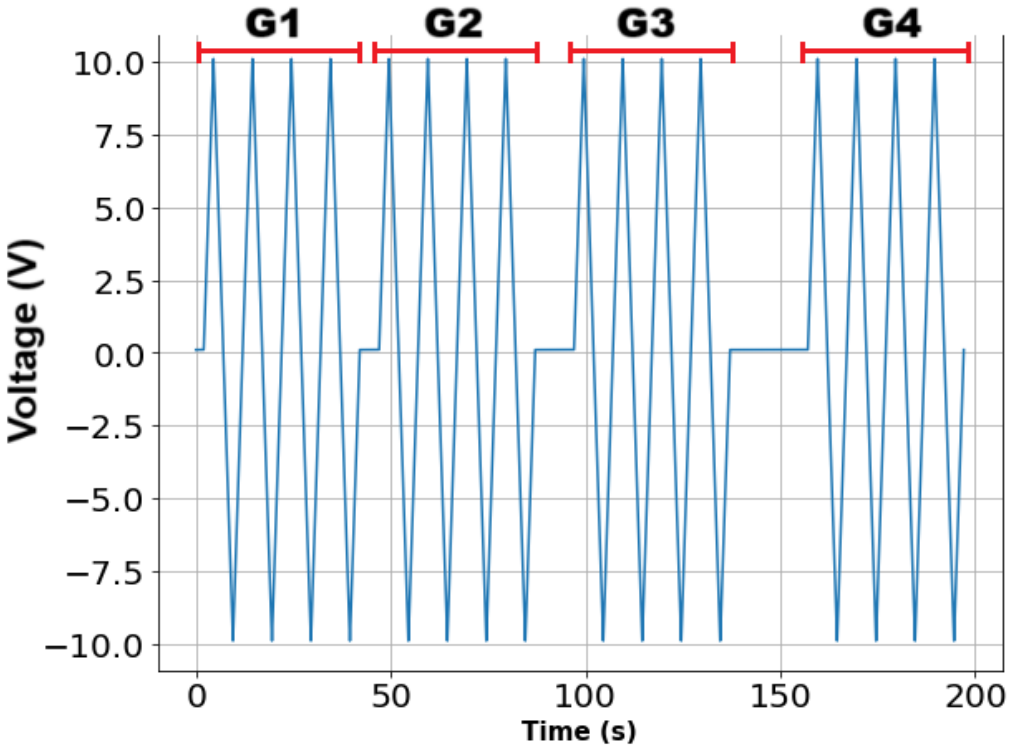

Source: Created by the author.

Figure 17 – Current-voltage (IV) curves were acquired at the three distinct points identified in Figure 14a. a) Point 1 (p1), b) Point 2 (p2) and c) Point (p3).

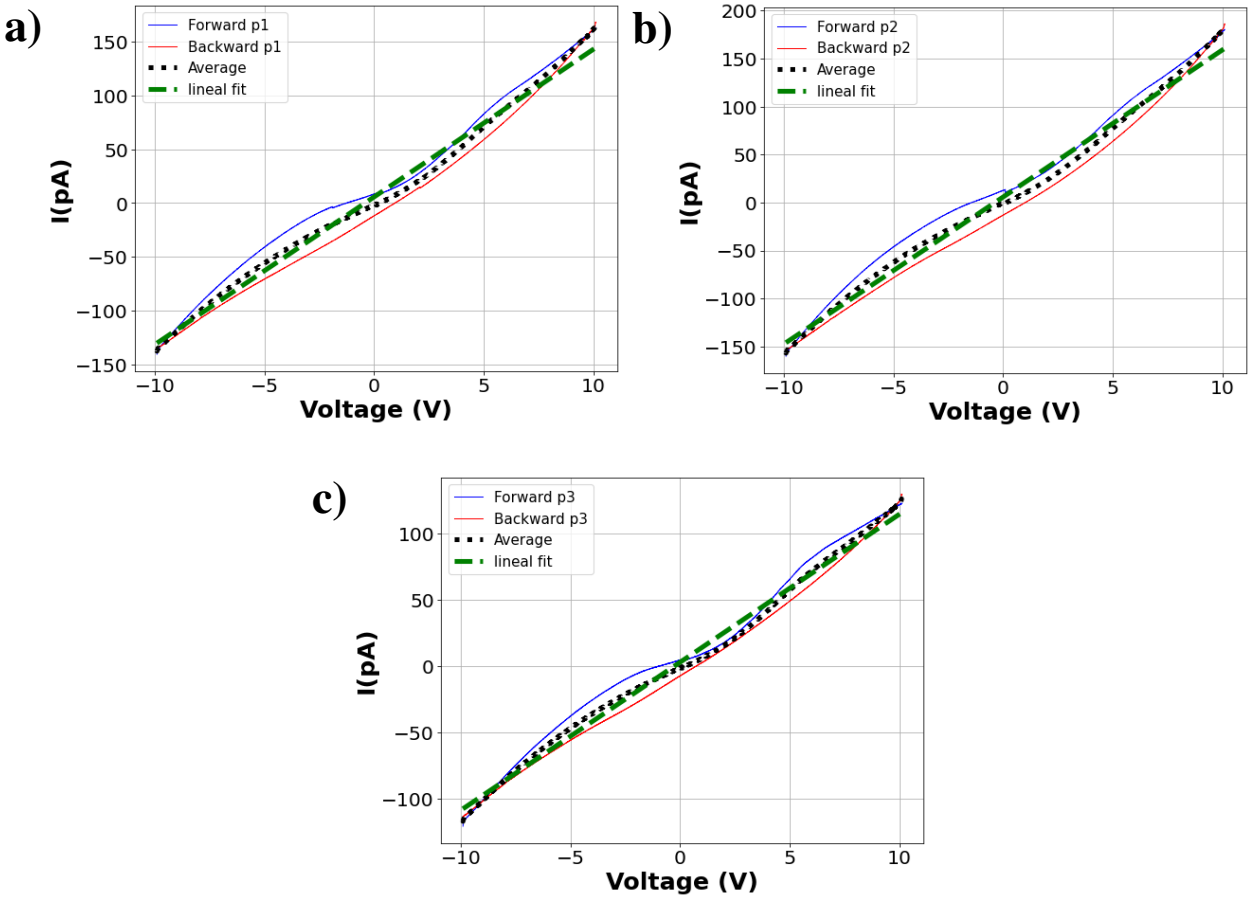

Source: Created by the author.

average value of 105.72 GΩ. These results indicate that the components of the internal structure of the L929 cell significantly influence charge transport and, consequently, the cell's electrical activity. The values found are one to two orders of magnitude higher than those reported for fibroblasts membrane in (Kamkin *et al.*, 1999) and (Kamkin *et al.*, 2001), where values of a few GΩ were reported.

For the calculation of capacitance, the system was modeled as an RC circuit in parallel with a constant capacitance and resistance. Furthermore, the electrical resistance of the substrate, which would be a component in series with the circuit, is at least five orders of magnitude lower than that of the cell and can therefore be neglected. The effect of displacement current due to the capacitance between the substrate and the cantilever was removed as indicated in (Rommel *et al.*, 2013).

The forward and backward scan currents, $i_{forward}$ and $i_{backward}$, can be described as

Figure 18 – Resistance distribution in three different points of the L929 Cell with $n_{p1} = 12$, $n_{p2} = 11$, and $n_{p3} = 11$.

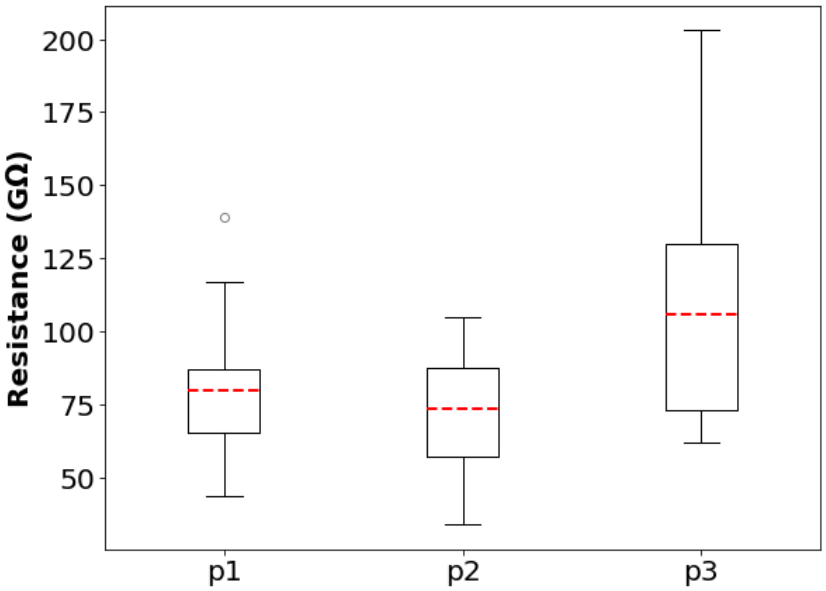

Source: Created by the author.

follows,

$$i_{forward} = \frac{V}{R} + C\nu, \tag{4.1}$$

$$i_{backward} = \frac{V}{R} - C\nu. \tag{4.2}$$

Thus, the capacitance can be calculated as

$$C = \frac{\Delta i}{2\nu} \tag{4.3}$$

where Δi is $i_{backward} - i_{forward}$, C is the capacitance, V the applied voltage, ν the voltage sweep rate, and R the resistance.

Figure 19 illustrates the distribution of capacitances calculated using Eq. (4.3). The mean capacitance values for points P1 and P2 were 2.40 pF and 2.73 pF, respectively, both showing remarkable similarity. For point P3, the capacitance was measured at 1.37 pF. These findings are slightly lower than those reported in (Shibukawa *et al.*, 2005), where the capacitance in cardiac fibroblasts was recorded as 4.5 ± 0.4 pF. Overall, the results indicate that the L929 cells have a high electrical resistance and low capacitance, suggesting that the system is characterized by a limited current flow and low charge storage capacity.

Figure 19 – Capacitance distribution in three different points of the L929 Cell with $n_{p1} = 12$, $n_{p2} = 11$, and $n_{p3} = 11$.

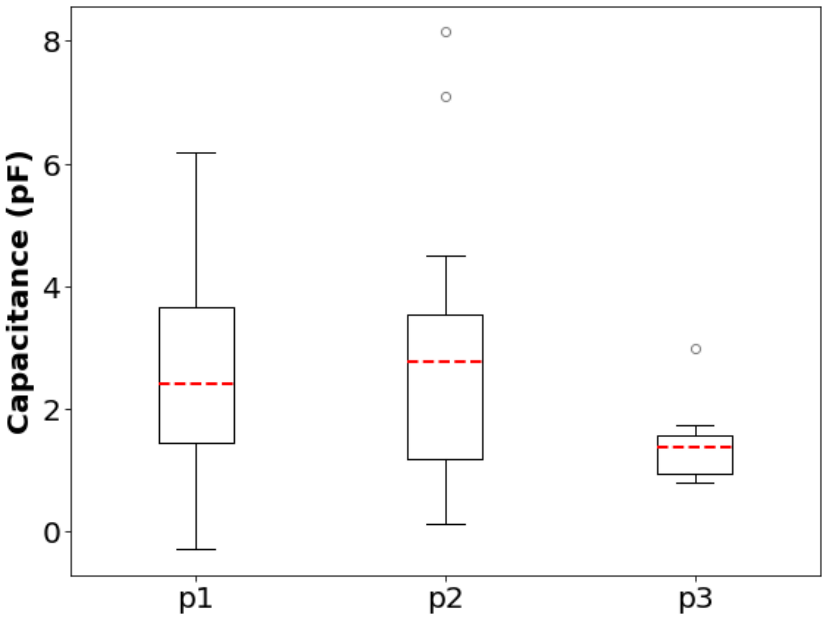

Source: Created by the author.

4.4 Electrical Conductivity in OFCOL II Cells Investigated by C-AFM

The experimental setup and measurements conducted for studying the electrical conductivity in the OFCOL II cell were identical to those used for the L929 cell.

Upon comparison of the topographical image of the OFCOL II cell with fluorescence microscopy images, it is evident that the nuclear region aligns with the highest part of the cell, as indicated by the green rectangle in Fig. 20a. The blue-highlighted region represents the cell extremity, which exhibits a high density of actin filaments according to Fig. 13b. Figure 20b presents the current distribution across the cell when the substrate is biased at 5 volts relative to the tip. This image highlights that the nuclear region has higher conductivity than the extremity of the cell body.

The average length of the cells was 44.31 $\pm$ 1.9 μm (N=12), and the average width was 25.31 $\pm$ 0.89 μm (N=12). These dimensions agree with previously reported sizes for osteoblast cells, which typically range from 20 to 50 micrometers (Qiu *et al.*, 2019). The average height of the cells was 720.05 $\pm$ 61.2 nm (N=12), slightly lower than the average height observed in L929 cells.

In the nuclear region, a rounded zone of greater height was identified, which, similar to the L929 cells, corresponds to the nucleolus and is marked as p1 in Fig. 20a. The remaining nuclear area is denoted as p2 in Fig. 20b. Figure 20c presents the height and current profiles

Figure 20 – Electrical conductivity in OFCOL II cells investigated by C-AFM a) Topography image of the OFCOL II cell. b) Image of the OFCOL II cell. c) Current and Height profile of line red in a).

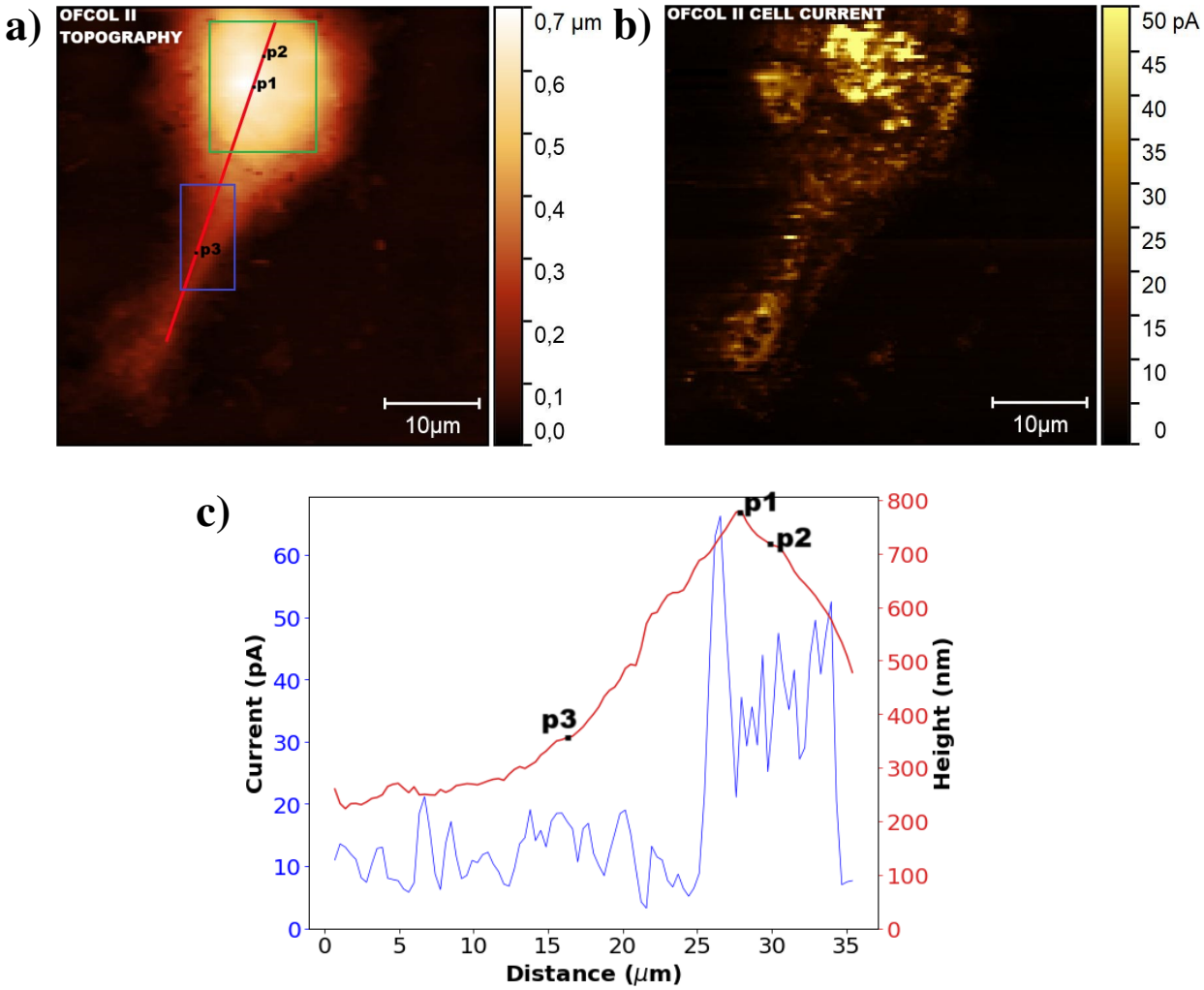

Source: Created by the author.

traced along the red line in Fig. 20a. This profile shows a correlation between the nuclear region and an increase in current relative to the rest of the cell body.

The histograms in Figs. 21a and 21b depict the current distribution within the nuclear region and the cell extremity, respectively. The average current in the nuclear region was 21.85 $\pm$ 4.83 pA (N=12), whereas in the cell extremity, it was 7.90 $\pm$ 0.92 pA (N=12). Although the average current observed is slightly lower than that measured in L929 cells, it demonstrates a consistent trend of increased current in the nuclear region.

Charge transport was investigated in various cell regions through I-V curves measured at points 1, 2, and 3, as depicted in Fig. 24. The I-V parameters employed were consistent with those used for L929 cells. The forward sweep (from -10 to 10 V) and the reverse sweep (from

Figure 21 – Current distribution in: a) the nuclear region and b) the extremity of the OFCOL II cell body.

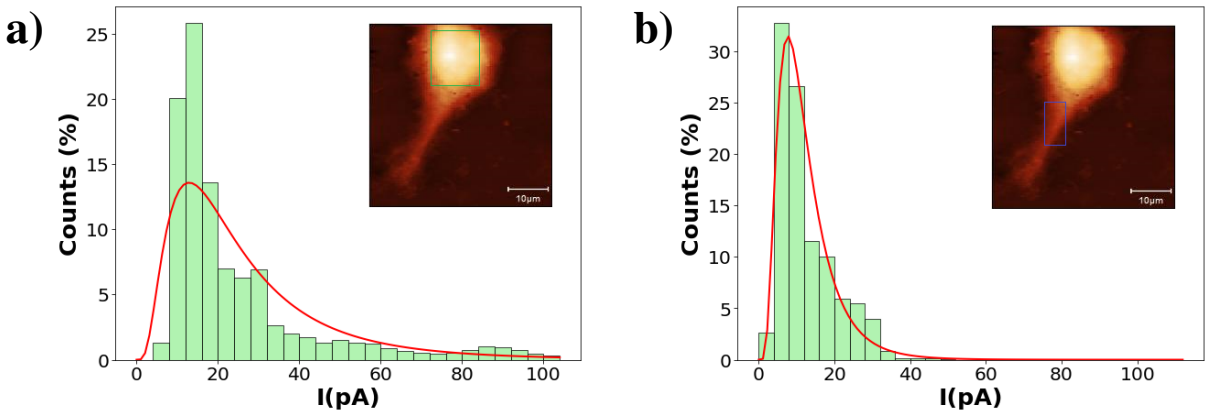

Source: Created by the author.

10 to -10 V) exhibited non-linear characteristics. A significant feature observed is a dramatic increase in current when positive polarization is applied. Additionally, during the reverse voltage sweep, the current follows a different path than the forward sweep, highlighting hysteresis effects attributed to a non-constant capacitance in this context. It is also noted that the current during the reverse sweep initially drops to a minimum before rising to its initial or saturation value.

In Fig. 24, it is evident that the current at point 1 is the highest, whereas point 3 exhibits a significantly lower current. Despite the generally similar behavior of the I-V curves across all three points, the non-linear current response and the reduced current at point 3 suggest that the displacement current due to capacitance predominantly affected the measurements. The correction procedure applied, as described in (Rommel *et al.*, 2013), resulted in many curves displaying unstable behavior and high noise levels. Consequently, the analysis for point 3 was performed with a more rigorous selection process, leading to a considerably smaller dataset than points 1 and 2.

The average of the forward and backward curves was computed in an initial analysis of the general behavior of the I-V curves. This averaged result was fitted using the diode equation for a solar cell (Bisquert *et al.*, 2021), as given by

$$I = I_0(e^{AV} - 1), \tag{4.4}$$

where I is the total current, $I_0 = \frac{nk_BT}{qR_0}$, and $A = \frac{q}{nk_BT}$, with q, k_B, T, n, and R_0 representing the elementary charge, Boltzmann constant, temperature, diode ideality factor, and resistance, respectively. The green line in Fig. 24 represents the fit. Only curves with an R^2>0.98 were considered for statistical purposes.

Figure 22 – Current-voltage (IV) curves were acquired at the three distinct points identified in Figure 20a. a) Point 1 (p1), b) Point 2 (p2) and c) Point (p3).

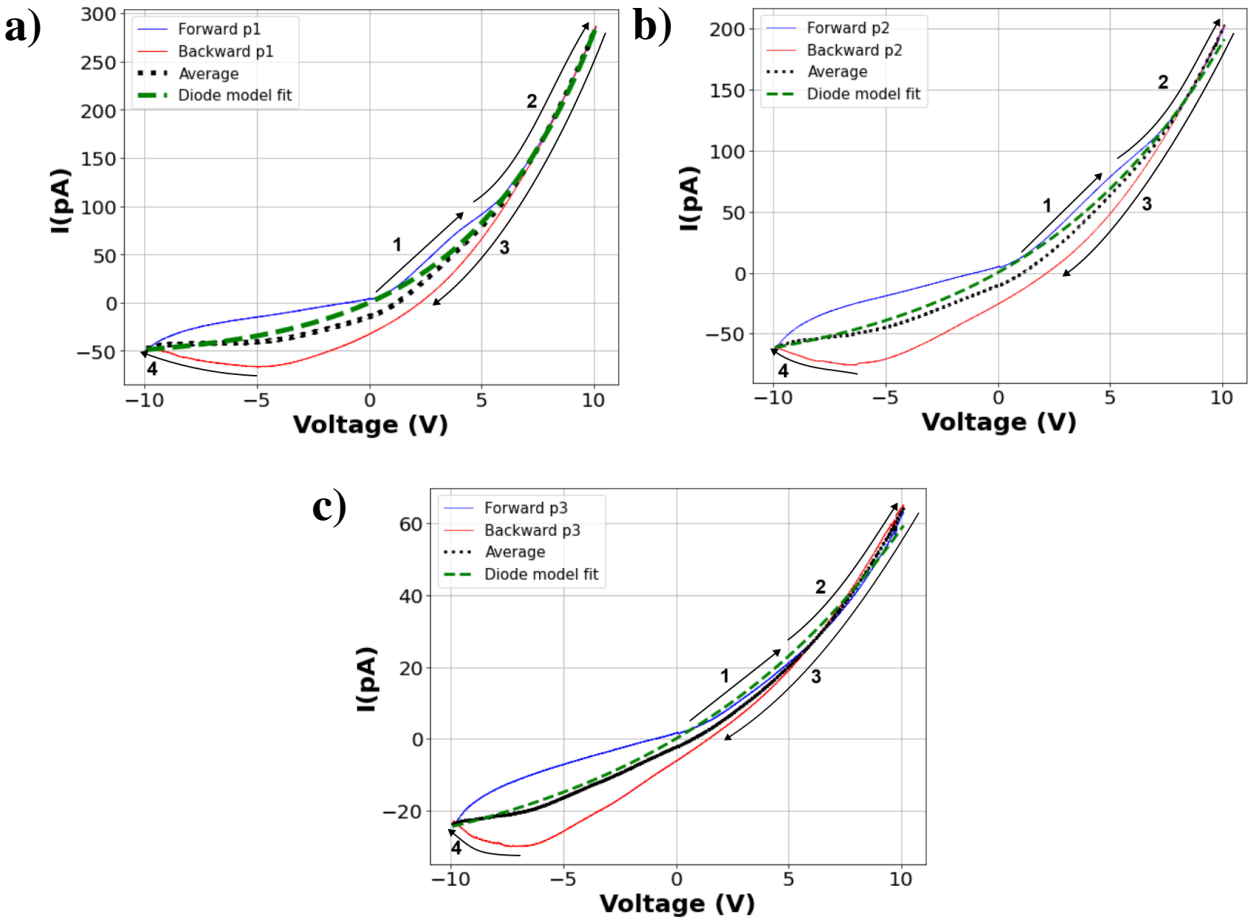

Source: Created by the author.

The resistance can thus be calculated as $R_0 = \frac{1}{I_0 A}$. Figure 23 displays the distribution of resistances for each specified point. The mean resistance values for $p1$, $p2$, and $p3$ were 119 GΩ, 158 GΩ, and 558 GΩ, respectively. While impedance studies on osteoblasts have been performed to evaluate their adhesion and proliferation (Giner *et al.*, 2020), and the resistance of a monolayer of osteoblasts analogous to epithelial layers has been reported as 1400 Ω cm^2 (Larrouture *et al.*, 2021), there are no direct measurements reported of the electrical resistance of the entire cell or its membrane.

The resistance R_0 obtained for the OFCOL II cell demonstrated an increase as the cell height decreased. This phenomenon may be related to the internal composition of the various cellular regions. Notably, resistance increased significantly at point 3, corresponding to a region with a high density of actin filaments. The arrangement of these filaments can influence charge propagation within the cell, as the resistance varies depending on whether the current flows transversely or longitudinally through the filaments (Hunley; Marucho, 2022).

Figure 23 – Resistance distribution in three different points of the OFCOL II Cell with $n_{p1} = 12$, $n_{p2} = 12$, and $n_{p3} = 6$.

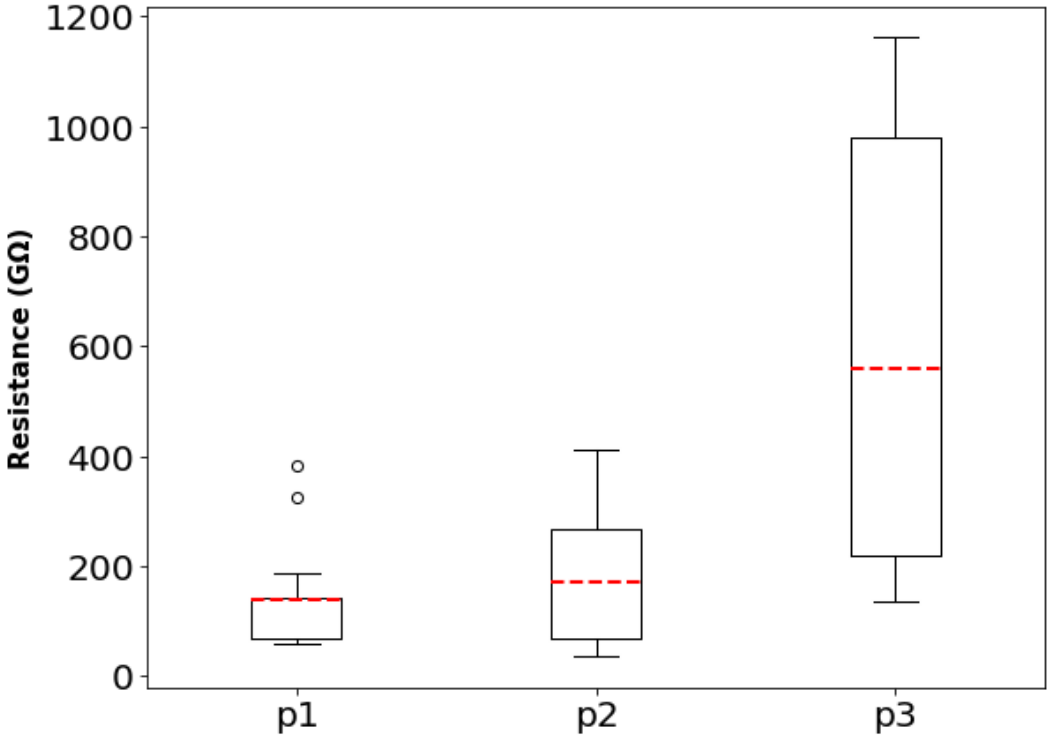

Source: Created by the author.

The non-linear nature of the I-V curves depicted in Fig. 24 suggests that the resistance is not constant but exhibits a voltage-dependent behavior, decreasing as the applied voltage increases. A suitable approximation for this voltage-dependent resistance, as detailed in (Bisquert *et al.*, 2021), is provided by

$$R(V) = R_0(e^{-AV}). \tag{4.5}$$

4.4.1 Analysis by sections

The I-V curves in Fig. 24 illustrate both forward and backward sweeps. Despite their high non-linearity, distinct behaviors can be observed across the curve. Four sections are highlighted in each curve to study which model best describes the charge transport characteristics in each indicated region.

Section 1 is where the current exhibits a sharp transition, moving from an almost constant value near zero to a linear dependence on the applied voltage. This shift in conduction mode suggests the presence of potential barriers formed by the tip-cell-ITO interface. The observed linear behavior implies ohmic transport, which can be characterized by the so-called

hopping mechanisms (Triyono *et al.*, 2020),

$$I(V) = \frac{V}{R_0}(e^{-\frac{E_a}{k_B T}}) \tag{4.6}$$

adhering to the Arrhenius relationship described by Eq. (4.6), where E_a is the activation energy, k_B is the Boltzmann constant, T is the temperature, and V is the applied voltage (DiBenedetto *et al.*, 2009).

Figure 24 – Current-voltage (IV) curves were acquired at the three distinct points identified in Figure 20a. a) Point 1 (p1), b) Point 2 (p2) and c) Point (p3).

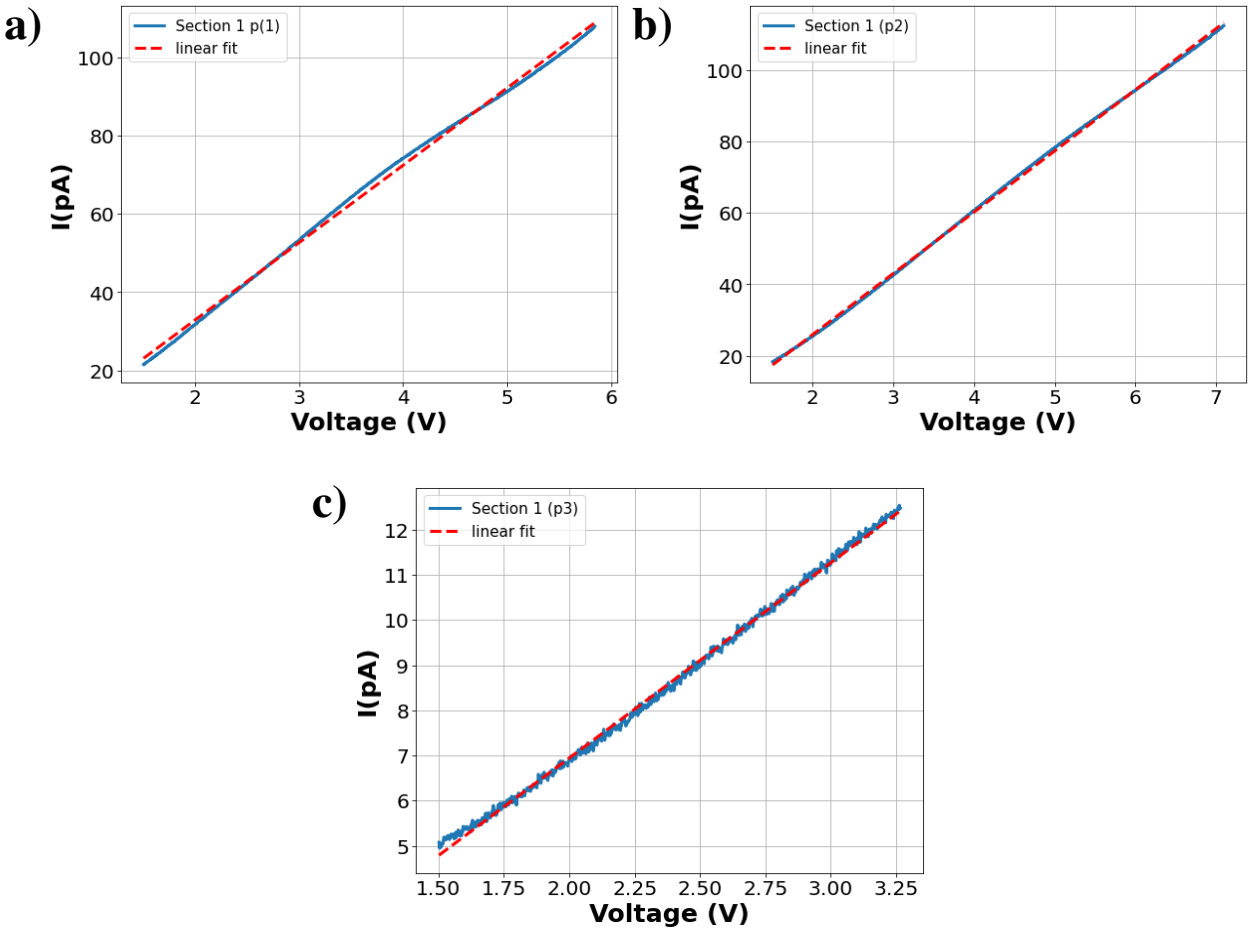

Source: Created by the author.

Figure 25 presents the linear fit for Section 1 at each measured point of the OFCOL II cell. Using the resulting slopes and Eq. (4.6), the activation energies were determined to be 0.017 ± 0.002 eV, 0.017 ± 0.002 eV, and 0.003 ± 0.0009 eV for points 1, 2, and 3, respectively. The detected activation energies suggest that, within this range, the cell behaves as a p-type semiconductor, with charge transport governed by hopping mechanisms (Triyono *et al.*, 2020).

Due to the ohmic behavior of Section 1, the resistance in this region can be calculated using the slopes obtained from the linear fits depicted in Figure 25. The resulting resistances

were 61.6± 7 GΩ, 74.6 ± 10.4 GΩ, and 321.82 ± 107.3 GΩ for points 1, 2, and 3, respectively. As expected, these values are lower than those obtained using the solar cell diode model since the equation indicates that the resistance in this region should decrease relative to R_0.

In the transition from Section 1 to Section 2, a slight decrease in the conductivity slope is observed, followed by a sharp increase, suggesting a change in the charge propagation mechanism in this region. The Schottky emission model was applied to investigate conductivity in this region. Given that the field intensity is less than 10^{-8} V/cm and the temperature is below 3000°C, this model can be applied without issue (Murphy; Good, 1956). The model can be expressed by the following equation

$$I(V) \propto exp(\frac{\beta\sqrt{V}}{k_B T} - \frac{\phi}{k_B T}), \tag{4.7}$$

$$\beta = \sqrt{q^3/4\pi\varepsilon d}, \tag{4.8}$$

where q is the electron charge, $k_B$is Boltzmann's constant, T is the absolute temperature, Φ is the junction barrier height, V is the voltage, d is the sample thickness, and ε is the permittivity (Guo *et al.*, 2018).

The Schottky emission model was applied to Section 2 of the I-V curves, and corresponding plots of $ln(I)$ versus $\sqrt{V}$ were generated. Using the resulting slopes and applying Eq. (4.8), the relative permittivity ε_r for each point was calculated. The absolute permittivity is defined as $\varepsilon = \varepsilon_0\varepsilon_r$.

The distribution of relative permittivities obtained is shown in Fig. 26, with mean values of 2.1, 3.24, and 4.28 for points 1, 2, and 3, respectively. These results indicate that point 3 exhibits a higher relative dielectric constant than the other cell points. This result could be attributed to the fact that the cell is predominantly composed of the plasma membrane at this location, which significantly enhances charge storage on the surface. Additionally, the plasma membrane contains a high concentration of proteins, and the value obtained is quite close to the commonly reported value for proteins (Guo *et al.*, 2018).

These results contrast with those reported in (Checa *et al.*, 2021) for HeLa cells, where the dielectric constant was measured via Scanning Dielectric Force Volume Microscopy. Those results show an increase in ε_r in the membrane region and a decrease in the nuclear region. However, this discrepancy may be attributed to both the sample and the experiment's nature.

Nonlinear conduction can also be explained by the Space-Charge Limited Current (SCLC) model, which mathematically provides a voltage-dependent current in the form of a

Figure 25 – Schottky Model Applied to the I-V Curves of the OFCOL II Cell: a) p1, b) p2, and c) p3

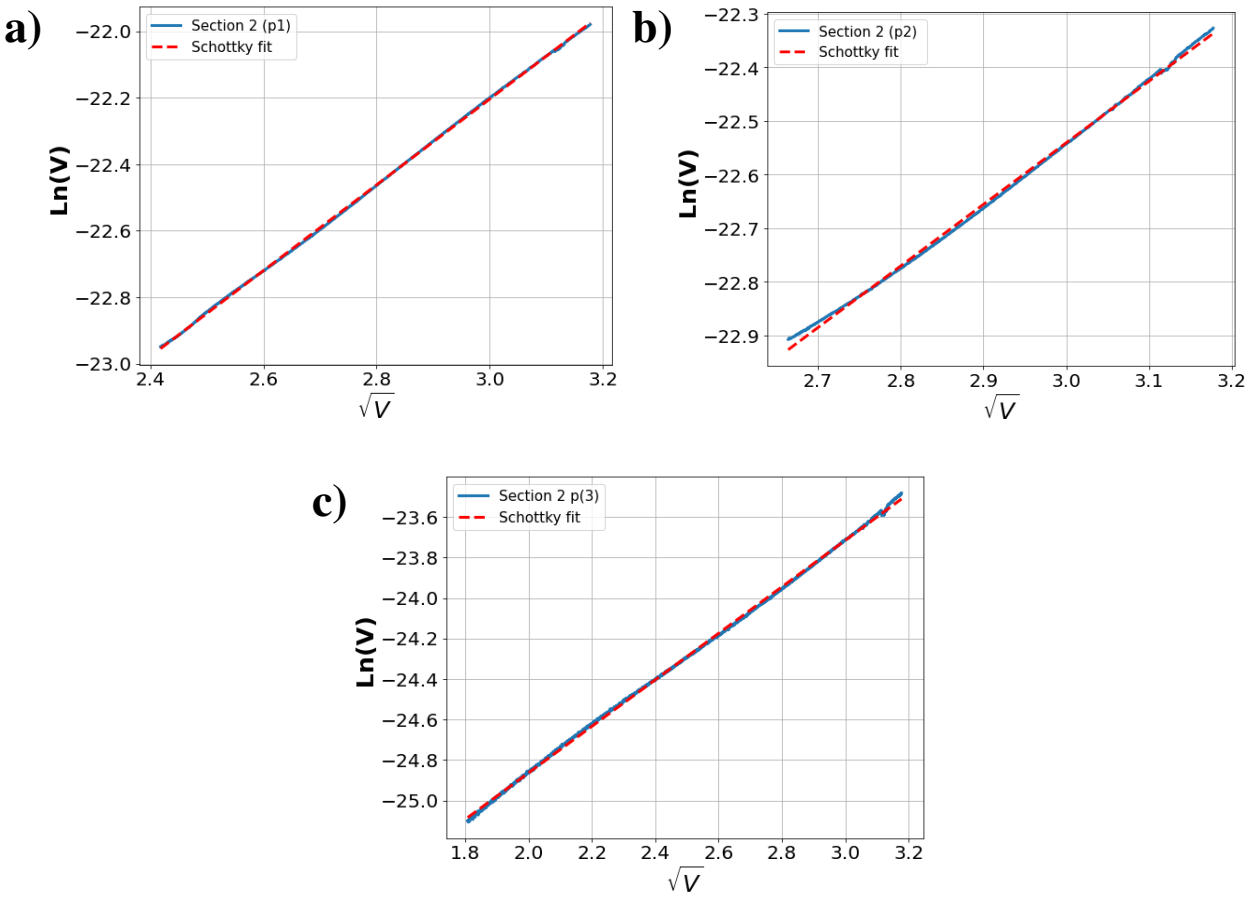

Source: Created by the author.

power-law relationship, $I \propto V^{\alpha}$ (Islam *et al.*, 2014). In semiconductor materials, the quadratic voltage dependence within this model is typically valid for voltages that are neither extremely low nor excessively high. Equation 4.9 describes the Mott–Gurney law, whose limitations and validity have been well-studied within the SCLC model (Murgatroyd, 1970),

$$I(V) = \frac{9}{8}\mu_p A \varepsilon \frac{V^2}{d^3}, \tag{4.9}$$

where μ_p is the charge carrier mobility, ε is the absolute permittivity, A is the effective area, d is the sample thickness, and V is the applied voltage.

The Mott-Gurney law will be applied to study the behavior of section 3. Figure 27 shows the application of this law to the I-V curves at each of the three points on the cell. The fitting was performed with the form BV^2, and the coefficient B was extracted to determine the charge carrier mobility. In the curves, it can be observed that the fit is not as good at shallow fields as it is at higher electric fields, as shown in (Röhr *et al.*, 2018).

To compute the mobility, the following considerations were made: the sample was

Figure 26 – Distribution of relative permittivity in OFCOL II Cells for three different points

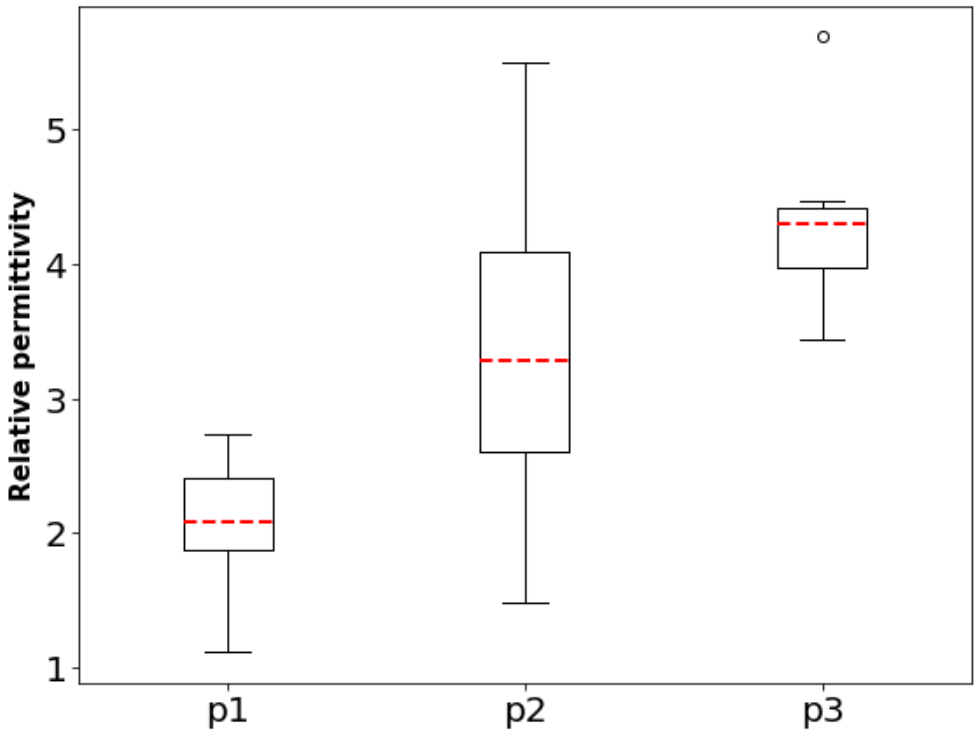

Source: Created by the author.

treated as an insulator. Thus the contact area is assumed to be equal to the emission area, $A_c = A_{eff}$ (Ruskell *et al.*, 1996). When the cell is fixed, its stiffness modulus E_H can be up to an order of magnitude greater than that of the live cell (Leporatti *et al.*, 2009). Based on results presented in (Lima *et al.*, 2024), where the OFCOL II cell showed a stiffness modulus slightly higher than that of L929 cell, and considering that in the L929 cell, the elastic modulus under fixation with 4% paraformaldehyde was approximately 4.5 times greater than in the live cell (Kim *et al.*, 2017), we estimate the elastic modulus of the fixed OFCOL II cell to be 18 kPa for our calculations. Finally, it is important to note that the elastic modulus of the tip, which is 322.8 GPa (Chien *et al.*, 2012), is significantly higher than that of the cell. Therefore, the contact area is described by the following equation,

$$A_c = \pi \left(F_c R_t \frac{3}{4} \frac{(1-\nu^2)}{E_H} \right)^{2/3}, \tag{4.10}$$

where F_c is the contact force, R_t is the tip radius, E_H is the Young's modulus of the cell, and ν_c is the Poisson's ratio of the cell, typically assumed to be 0.5 (Jastrzebski, 1959). The mobility values were $1.03 \pm 0.18 \times 10^{-6}\,\mathrm{m^2/Vs}$, $0.3 \pm 0.06 \times 10^{-6}\,\mathrm{m^2/Vs}$, and $2.73 \pm 0.49 \times 10^{-8}\,\mathrm{m^2/Vs}$ for points p1, p2, and p3, respectively. The results are consistent with expectations, as the resistance for p3 was higher, which translates to lower charge mobility than the other two points, which

Figure 27 – Mott-Gurney law fitted to the I-V Curves of the OF-COL II Cell: a) p1, b) p2, and c) p3.

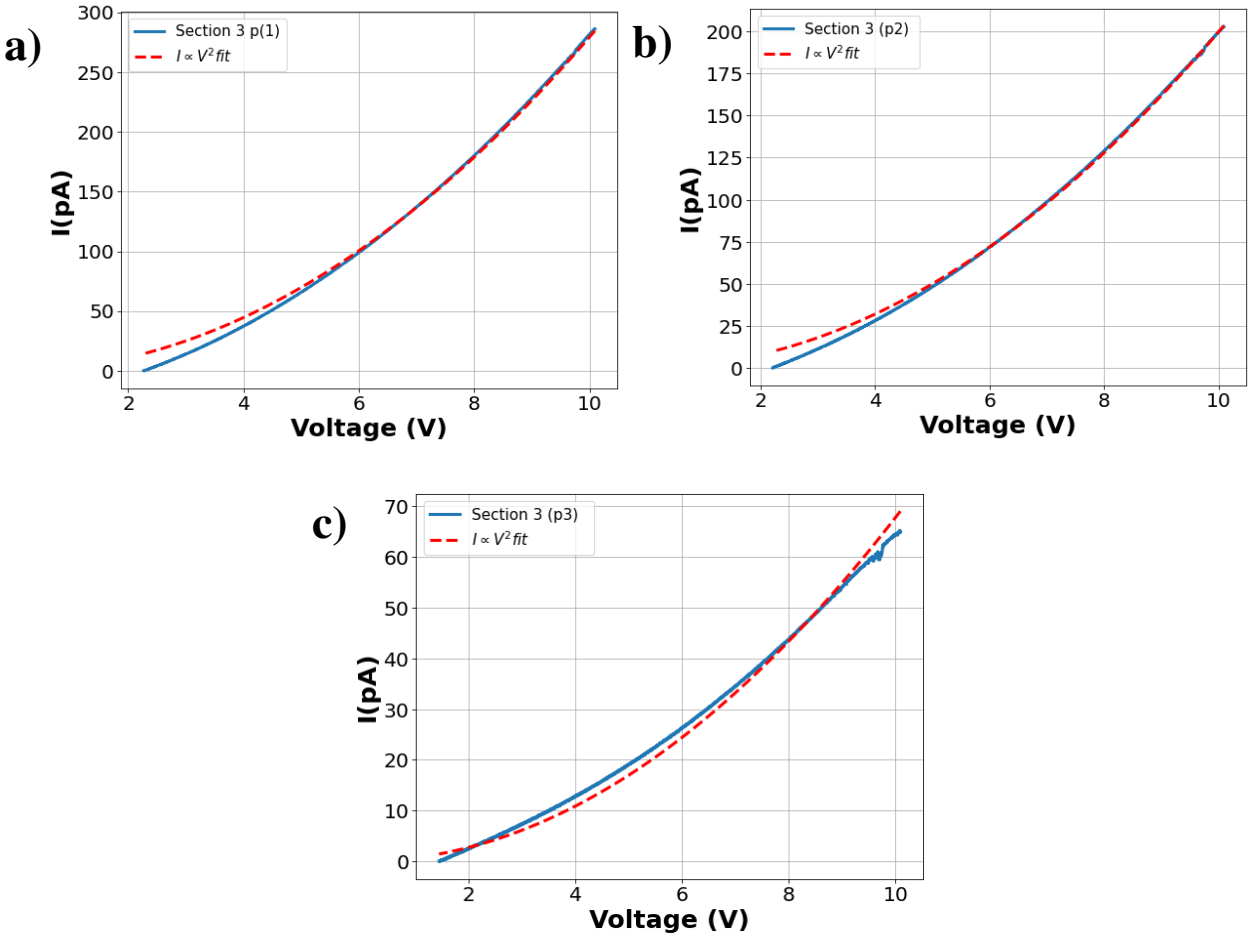

Source: Created by the author.

exhibited similar mobilities. The results for this point are consistent in magnitude with those reported for proteins in (Ma *et al.*, 2020). Generally, the mobility within the cell is low compared to organic semiconductors such as pentacene (Hutsch *et al.*, 2022).

The final region to highlight is Section 4, where a significant hysteresis is observed in the backward curve, where the current initially drops to a minimum value and then increases linearly as the voltage decreases. This effect is negative differential resistance NDR (Mikolajick *et al.*, 2022). This phenomenon is commonly found in semiconductor devices, where the NDR is often attributed to quantum effects, such as tunneling. It was initially documented in tunnel diodes (Grobis *et al.*, 2005).

The coexistence of memory effects with negative differential resistance (NDR) has also been documented in various devices (Zhou *et al.*, 2018). NDR has been utilized in applications such as transistors, frequency multipliers, and high-frequency oscillators and has also been observed in numerous organic semiconductors (Zhu *et al.*, 2019). This phenomenon

is evident in the graphs shown in Fig. 24 where, in addition to NDR, the observed hysteresis indicates memory behavior across all points within the cell. Both hysteresis and NDR are more pronounced in the nuclear region of the cell. These results suggest that, within this voltage range, the cell is capable of more excellent charge storage.

5 CONCLUSIONS AND FUTURE WORK

This thesis established a robust and reliable protocol for studying electrical conductivity directly in cells, enabling the successful execution of Conductive Atomic Force Microscopy (C-AFM) measurements. The protocol's robustness effectively minimized potential sources of interference and achieved sufficient repeatability for comprehensive data analysis, inspiring confidence in the research methodology. The L929 fibroblast cell line and the OFCOL II osteoblast cell line exhibited distinct electrical behaviors when subjected to AC voltage, likely related to their differing biomolecular compositions. While fibroblasts generally displayed ohmic behavior, osteoblasts exhibited highly non-linear conductivity. Under DC voltage, the current passing through fibroblasts was slightly higher. Despite exhibiting different charge transport mechanisms, both the L929 and OFCOL II cell lines demonstrated higher conductivity at the nucleus than other cell body regions. This study successfully quantified specific local electrical properties directly in cells, highlighting the potential for detecting changes in the internal composition of cells and evaluating cell adhesion and topographical changes as the understanding of charge transport mechanisms in different biomolecules advances. The conduction mechanisms observed in the OFCOL II cells exhibit behavior strikingly similar to that seen in specific electronic device systems. This similarity opens up exciting possibilities for future research and industrial applications of cellular models, inspiring hope for further advancements. This work marks the preliminary phase of a more extensive investigation into cell electrical properties. The protocol developed in this study is expected to be applied to cells under various physicochemical conditions to evaluate their impact on cellular electrical behavior. Furthermore, this technique can be augmented with other AFM modes, such as Scanning Kelvin Probe Microscopy and Electrostatic Force Microscopy, to provide a more comprehensive understanding of cellular electrical properties.

REFERENCES

ALBERTS, B.; WILSON, J.; HUNT, T. **Molecular Biology of the Cell**. Garland Science, 2008. ISBN 9780815341116. Available at: https://books.google.com.br/books?id=iepqmRfP3ZoC. Accessed on: 15 May 2024.

ARMSTRONG, D. L.; ERXLEBEN, C.; WHITE, J. A. Chapter 7 - patch clamp methods for studying calcium channels. *In*: WHITAKER, M. (ed.). **Calcium in Living Cells**. [*s.l*]: Academic Press, 2010, (Methods in Cell Biology, v. 99). p. 183–197.

ASAMI, K. Characterization of heterogeneous systems by dielectric spectroscopy. **Progress in Polymer Science**, [*s.l*], v. 27, n. 8, p. 1617–1659, 2002. ISSN 0079-6700. doi:10.1016/S0079-6700(02)00015-1.

BERS, D. M. Cardiac excitation–contraction coupling. **Nature**, [*s.l*], v. 415, n. 6868, p. 198–205, jan 2002. ISSN 1476-4687. doi:10.1038/415198a.

BIRKENHAUER, E.; NEETHIRAJAN, S. Surface potential measurement of bacteria using kelvin probe force microscopy. **J. Vis. Exp.**, [*s.l*], n. 93, p. e52327, nov. 2014. doi:10.3791/52327.

BISQUERT, J.; GUERRERO, A.; GONZALES, C. Theory of hysteresis in halide perovskites by integration of the equivalent circuit. **ACS Phys. Chem. Au**, [*s.l*], v. 1, n. 1, p. 25–44, nov. 2021.

BOUNIK, R.; CARDES, F.; ULUSAN, H.; MODENA, M. M.; HIERLEMANN, A. Impedance imaging of cells and tissues: design and applications. **BME Frontiers**, [*s.l*], v. 2022, p. 9857485, 2022. doi:10.34133/2022/9857485.

CARVALHO, J. A bioelectric model of carcinogenesis, including propagation of cell membrane depolarization and reversal therapies. **Sci. Rep.**, [*s.l*], v. 11, n. 1, p. 13607, jun. 2021.

CHECA, M.; MILLAN-SOLSONA, R.; MARES, A. G.; PUJALS, S.; GOMILA, G. Fast label-free nanoscale composition mapping of eukaryotic cells via scanning dielectric force volume microscopy and machine learning. **Small Methods**, [*s.l*], v. 5, n. 7, p. e2100279, jul. 2021.

CHEN, Z.; LI, W.; LI, R.; ZHANG, Y.; XU, G.; CHENG, H. Fabrication of highly transparent and conductive indium–tin oxide thin films with a high figure of merit via solution processing. **Langmuir**, [*s.l*], v. 29, n. 45, p. 13836–13842, 2013. doi:10.1021/la4033282.

CHEONG, L.-Z.; ZHAO, W.; SONG, S.; SHEN, C. Lab on a tip: Applications of functional atomic force microscopy for the study of electrical properties in biology. **Acta Biomaterialia**, [*s.l*], v. 99, p. 33–52, 2019. ISSN 1742-7061. doi:10.1016/j.actbio.2019.08.023.

CHIEN, H. H.; MA, K. J.; KUO, C. H. The mechanical properties of platinum-iridium alloy coating. **Adv. Mat. Res.**, [*s.l*], v. 486, p. 533–537, mar. 2012.

COHEN, H.; NOGUES, C.; NAAMAN, R.; PORATH, D. Direct measurement of electrical transport through single DNA molecules of complex sequence. **Proc Natl Acad Sci U S A**, United States, v. 102, n. 33, p. 11589–11593, aug. 2005. doi:10.1073/pnas.0505272102.

COLE, K. S. **Membranes, Ions, and Impulses**. Reprint 2020. [s.l.]: University of California Press, 2020. (Biophysics Series; 1). ISBN 9780520326514; 0520326512.

COOPER, G. M. **Structure and Organization of Actin Filaments**. Sunderland, MA: Sinauer Associates, 2000.

DIBENEDETTO, S. A.; FACCHETTI, A.; RATNER, M. A.; MARKS, T. J. Charge conduction and breakdown mechanisms in self-assembled nanodielectrics. **J. Am. Chem. Soc.**, [*s.l*], v. 131, n. 20, p. 7158–7168, may 2009.

EL-NAGGAR, M. Y.; WANGER, G.; LEUNG, K. M.; YUZVINSKY, T. D.; SOUTHAM, G.; YANG, J.; LAU, W. M.; NEALSON, K. H.; GORBY, Y. A. Electrical transport along bacterial nanowires from shewanella oneidensis MR-1. **Proc. Natl. Acad. Sci. U. S. A.**, [*s.l*], v. 107, n. 42, p. 18127–18131, oct. 2010.

GARRILL, A.; DAVIES, J. M. Patch clamping fungal membranes: a new perspective on ion transport. **Mycological Research**, [*s.l*], v. 98, n. 3, p. 257–263, 1994. ISSN 0953-7562. doi:10.1016/S0953-7562(09)80452-8.

GINER, M.; OLMO, A.; HERNÁNDEZ, M.; TRUEBA, P.; CHICARDI, E.; CIVANTOS, A.; VÁZQUEZ, M. Á.; MONTOYA-GARCÍA, M.-J.; TORRES, Y. Use of impedance spectroscopy for the characterization of in-vitro osteoblast cell response in porous titanium bone implants. **Metals (Basel)**, [*s.l*], v. 10, n. 8, p. 1077, aug. 2020.

GROBIS, M.; WACHOWIAK, A.; YAMACHIKA, R.; CROMMIE, M. F. Tuning negative differential resistance in a molecular film. **Appl. Phys. Lett.**, [*s.l*], v. 86, n. 20, p. 204102, may 2005.

GUO, T.; SUN, B.; ZHOU, Y.; ZHAO, H.; LEI, M.; ZHAO, Y. Overwhelming coexistence of negative differential resistance effect and RRAM. **Phys. Chem. Chem. Phys.**, [*s.l*], n. 31, 2018.

HAASE, K.; PELLING, A. E. Investigating cell mechanics with atomic force microscopy. **J. R. Soc. Interface**, [*s.l*], v. 12, n. 104, p. 20140970, mar. 2015.

HAMILL, O. P.; MARTY, A.; NEHER, E.; SAKMANN, B.; SIGWORTH, F. J. Improved patch-clamp techniques for high-resolution current recording from cells and cell-free membrane patches. **Pflugers Arch.**, [*s.l*], v. 391, n. 2, p. 85–100, aug. 1981.

HAN, A.; MOSS, E.; RABBITT, R. D.; FRAZIER, A. B. A multi-purpose micro system for electrophysiological analyses of single cells. *In*: BABA, Y.; SHOJI, S.; BERG, A. van den (ed.). **Micro Total Analysis Systems 2002**. Dordrecht: Springer Netherlands, 2002. p. 805–807. ISBN 978-94-010-0504-3.

HAN, A.; YANG, L.; FRAZIER, A. B. Quantification of the Heterogeneity in Breast Cancer Cell Lines Using Whole-Cell Impedance Spectroscopy. **Clinical Cancer Research**, [*s.l*], v. 13, n. 1, p. 139–143, 01 2007. ISSN 1078-0432. doi:10.1158/1078-0432.CCR-06-1346.

HILLE, B. **Ion channels of excitable membranes 2nd ed**. [s.l.]: SINAUER ASSOCIATES INC, 1991. ISBN 0-87892-323-9.

HODGKIN, A. L.; HUXLEY, A. F. A quantitative description of membrane current and its application to conduction and excitation in nerve. **The Journal of Physiology**, [*s.l*], v. 117, n. 4, p. 500–544, 1952. Available at: https://physoc.onlinelibrary.wiley.com/doi/pdf/10.1113/jphysiol.1952.sp004764. Accessed on: 28 Jun 2024.

HUNLEY, C.; MARUCHO, M. Electrical propagation of condensed and diffuse ions along actin filaments. **J. Comput. Neurosci.**, [*s.l*], v. 50, n. 1, p. 91–107, feb. 2022.

HUTSCH, S.; PANHANS, M.; ORTMANN, F. Charge carrier mobilities of organic semiconductors: ab initio simulations with mode-specific treatment of molecular vibrations. **Npj Comput. Mater.**, [*s.l*], v. 8, n. 1, nov. 2022.

ISLAM, S. M.; BANERJI, P.; BANERJEE, S. Electrical bistability, negative differential resistance and carrier transport in flexible organic memory device based on polymer bilayer structure. **Org. Electron.**, [*s.l*], v. 15, n. 1, p. 144–149, jan. 2014.

JASTRZEBSKI, Z. **Nature and Properties of Engineering Materials**. [s.l.]: Wiley, 1959. (Wiley international edition). ISBN 9780471440888.

KAMKIN, A.; KISELEVA, I.; WAGNER, K.; SCHOLZ, H.; THERES, H.; KAZANSKI, V.; LOZINSKY, I.; GÜNTHER, J.; ISENBERG, G. Mechanically induced potentials in rat atrial fibroblasts depend on actin and tubulin polymerisation. **Pflügers Archiv**, [*s.l*], v. 442, n. 4, p. 487–497, jul. 2001.

KAMKIN, A.; KISELEVA, I.; WAGNER, K. D.; LAMMERICH, A.; BOHM, J.; PERSSON, P. B.; GÜNTHER, J. Mechanically induced potentials in fibroblasts from human right atrium. **Exp. Physiol.**, [*s.l*], v. 84, n. 2, p. 347–356, mar. 1999.

KEYNES, R. D. Molecular biology and biophysics of ion channels. **BioEssays**, [*s.l*], v. 2, n. 3, p. 100–106, 1985. doi:10.1002/bies.950020303.

KIM, S.-O.; KIM, J.; OKAJIMA, T.; CHO, N.-J. Mechanical properties of paraformaldehyde-treated individual cells investigated by atomic force microscopy and scanning ion conductance microscopy. **Nano Converg.**, [*s.l*], v. 4, n. 1, p. 5, mar. 2017.

LANZA, M. **Conductive Atomic Force Microscopy**: Applications in nanomaterials. [s.l.]: Wiley-VCH Verlag GmbH Co., 2017. ISBN 978-3-527-69978-0.

LARROUTURE, Q. C.; TOURKOVA, I. L.; STOLZ, D. B.; RIAZANSKI, V.; ONWUKA, K. M.; FRANKS, J. M.; DOBROWOLSKI, S. F.; NELSON, D. J.; SCHLESINGER, P. H.; BLAIR, H. C. Growth and mineralization of osteoblasts from mesenchymal stem cells on microporous membranes: Epithelial-like growth with transmembrane resistance and ph gradient. **Biochem. Biophys. Res. Commun.**, [*s.l*], v. 580, p. 14–19, nov. 2021.

LAZANAS, A. C.; PRODROMIDIS, M. I. Electrochemical impedance spectroscopya tutorial. **ACS Measurement Science Au**, [*s.l*], v. 3, n. 3, p. 162–193, 2023. doi:10.1021/acsmeasuresciau.2c00070.

LEPORATTI, S.; VERGARA, D.; ZACHEO, A.; VERGARO, V.; MARUCCIO, G.; CINGOLANI, R.; RINALDI, R. Cytomechanical and topological investigation of MCF-7 cells by scanning force microscopy. **Nanotechnology**, [*s.l*], v. 20, n. 5, p. 055103, feb. 2009.

LIMA, I. V. M.; SILVA, A. V. S.; SOUSA, F. D.; FERREIRA, W. P.; FREIRE, R. S.; OLIVEIRA, C. L. N. de; SOUSA, J. S. de. Measuring the viscoelastic relaxation function of cells with a time-dependent interpretation of the Hertz-Sneddon indentation model. **Heliyon**, [*s.l*], v. 10, n. 10, p. e30623, may 2024.

LODISH, H.; BERK, A.; KAISER, C.; KRIEGER, M.; BRETSCHER, A.; PLOEGH, H.; MARTIN, K.; YAFFE, M.; AMON, A. **Molecular Cell Biology**. 5. ed. New York, NY: W.H. Freeman, 2008. ISBN 9780716743668.

MA, C.; GAO, X.; YANG, Y.; BIAN, X.; WANG, B.; LIU, X.; WANG, Y.; SU, D.; ZHANG, G.; QU, L.; ZHANG, N. The three-dimensional culture of L929 and C2C12 cells based on SPI-SA interpenetrating network hydrogel scaffold with excellent mechanical properties. **Front. Bioeng. Biotechnol.**, [*s.l*], v. 11, p. 1329183, 2023.

MA, G.; WAN, Z.; YANG, Y.; ZHANG, P.; WANG, S.; TAO, N. Optical imaging of single-protein size, charge, mobility, and binding. **Nat. Commun.**, [*s.l*], v. 11, n. 1, p. 4768, sep. 2020.

MALVANKAR, N. S.; YALCIN, S. E.; TUOMINEN, M. T.; LOVLEY, D. R. Visualization of charge propagation along individual pili proteins using ambient electrostatic force microscopy. **Nature Nanotechnology**, [*s.l*], v. 9, n. 12, p. 1012–1017, dec. 2014. doi:10.1038/nnano.2014.236.

MIKOLAJICK, T.; GALDERISI, G.; RAI, S.; SIMON, M.; BÖCKLE, R.; SISTANI, M.; CAKIRLAR, C.; BHATTACHARJEE, N.; MAUERSBERGER, T.; HEINZIG, A.; KUMAR, A.; WEBER, W. M.; TROMMER, J. Reconfigurable field effect transistors: A technology enablers perspective. **Solid State Electron.**, [*s.l*], v. 194, n. 108381, p. 108381, aug. 2022.

MOON, S.-H.; CHO, Y.-W.; SHIM, H.-E.; CHOI, J.-H.; JUNG, C.-H.; HWANG, I.-T.; KANG, S.-W. Electrically stimulable indium tin oxide plate for long-term in vitro cardiomyocyte culture. **Biomaterials Research**, [*s.l*], v. 24, n. 1, p. 10, May 2020. ISSN 2055-7124. doi:10.1186/s40824-020-00189-0.

MURGATROYD, P. N. Theory of space-charge-limited current enhanced by frenkel effect. **J. Phys. D Appl. Phys.**, [*s.l*], v. 3, n. 2, p. 151–156, feb. 1970.

MURPHY, E. L.; GOOD, R. H. Thermionic emission, field emission, and the transition region. **Phys. Rev.**, [*s.l*], v. 102, n. 6, p. 1464–1473, jun. 1956.

NEČAS, D.; KLAPETEK, P. Gwyddion: an open-source software for spm data analysis. **Central European Journal of Physics**, [*s.l*], v. 10, n. 1, p. 181–188, Feb 2012. ISSN 1644-3608. doi:10.2478/s11534-011-0096-2.

NEHER, E.; SAKMANN, B. Single-channel currents recorded from membrane of denervated frog muscle fibres. **Nature**, [*s.l*], v. 260, n. 5554, p. 799–802, Apr 1976. ISSN 1476-4687. doi:10.1038/260799a0.

OLIVEIRA, D. A. A. P.; OLIVEIRA, R. F. de; ZANGARO, R. A.; SOARES, C. P. Evaluation of low-level laser therapy of osteoblastic cells. **Photomed Laser Surg**, United States, v. 26, n. 4, p. 401–404, aug. 2008.

OLIVEIRA, R. D.; ALBUQUERQUE, D.; CRUZ, T.; YAMAJI, F.; LEITE, F. Measurement of the nanoscale roughness by atomic force microscopy: Basic principles and applications. *In*: BELLITTO, V. (ed.). **Atomic Force Microscopy**. Rijeka: IntechOpen, 2012. chap. 7.

PAIMAN, S.; Hui Ling, T.; HUSHAM, M.; SAGADEVAN, S. Significant effect on annealing temperature and enhancement on structural, optical and electrical properties of

zinc oxide nanowires. **Results in Physics**, [*s.l*], v. 17, p. 103185, 2020. ISSN 2211-3797. doi:10.1016/j.rinp.2020.103185.

PEDERSON, T. The nucleolus. **Cold Spring Harb. Perspect. Biol.**, [*s.l*], v. 3, n. 3, p. a000638–a000638, mar. 2011.

PETERSEN, C. C. Whole-cell recording of neuronal membrane potential during behavior. **Neuron**, [*s.l*], v. 95, n. 6, p. 1266–1281, 2017. ISSN 0896-6273. doi:10.1016/j.neuron.2017.06.049.

PHIPPS, R. P.; BORRELLO, M. A.; BLIEDEN, T. M. Fibroblast heterogeneity in the periodontium and other tissues. **J Periodontal Res**, United States, v. 32, n. 1 Pt 2, p. 159–165, jan. 1997.

PITTENGER, M. F.; MACKAY, A. M.; BECK, S. C.; JAISWAL, R. K.; DOUGLAS, R.; MOSCA, J. D.; MOORMAN, M. A.; SIMONETTI, D. W.; CRAIG, S.; MARSHAK, D. R. Multilineage potential of adult human mesenchymal stem cells. **Science**, United States, v. 284, n. 5411, p. 143–147, apr. 1999.

QIU, Z.-Y.; CUI, Y.; WANG, X.-M. Chapter 1 - natural bone tissue and its biomimetic. *In*: WANG, X.-M.; QIU, Z.-Y.; CUI, H. (ed.). **Mineralized Collagen Bone Graft Substitutes**. [s.l.]: Woodhead Publishing, 2019, (Woodhead Publishing Series in Biomaterials). p. 1–22. ISBN 978-0-08-102717-2.

RAICU, V.; POPESCU, A. Cell membrane: Structure and physical properties. *In*: RAICU, V.; POPESCU, A. (ed.). **Integrated Molecular and Cellular Biophysics**. Dordrecht: Springer Netherlands, 2008. p. 73–99. ISBN 978-1-4020-8268-9.

RIBATTI, D. An historical note on the cell theory. **Exp. Cell Res.**, [*s.l*], v. 364, n. 1, p. 1–4, mar. 2018.

RÖHR, J. A.; MOIA, D.; HAQUE, S. A.; KIRCHARTZ, T.; NELSON, J. Exploring the validity and limitations of the Mott–Gurney law for charge-carrier mobility determination of semiconducting thin-films. **J. Phys. Condens. Matter**, [*s.l*], v. 30, n. 10, p. 105901, mar. 2018.

ROMMEL, M.; JAMBRECK, J. D.; LEMBERGER, M.; BAUER, A. J.; FREY, L.; MURAKAMI, K.; RICHTER, C.; WEINZIERL, P. Influence of parasitic capacitances on conductive AFM *i-v* measurements and approaches for its reduction. **J. Vac. Sci. Technol. B Nanotechnol. Microelectron.**, [*s.l*], v. 31, n. 1, p. 01A108, jan. 2013.

ROURK, C. J. Indication of quantum mechanical electron transport in human substantia nigra tissue from conductive atomic force microscopy analysis. **Biosystems**, [*s.l*], v. 179, p. 30–38, 2019. ISSN 0303-2647. doi:10.1016/j.biosystems.2019.02.003.

RUSKELL, T. G.; WORKMAN, R. K.; CHEN, D.; SARID, D.; DAHL, S.; GILBERT, S. High resolution Fowler-Nordheim field emission maps of thin silicon oxide layers. **Appl. Phys. Lett.**, [*s.l*], v. 68, n. 1, p. 93–95, jan. 1996.

SAULIS, G. Electroporation of cell membranes: The fundamental effects of pulsed electric fields in food processing. **Food Eng. Rev.**, [*s.l*], v. 2, n. 2, p. 52–73, jun. 2010.

SCHWAN, H. P. Electrical properties of tissue and cell. **Advances in Biological and Medical Physics**, [*s.l*], v. 5, p. 147–209, 1957.

SHIBUKAWA, Y.; CHILTON, E. L.; MACCANNELL, K. A.; CLARK, R. B.; GILES, W. R. K+ currents activated by depolarization in cardiac fibroblasts. **Biophys. J.**, [*s.l*], v. 88, n. 6, p. 3924–3935, jun. 2005.

SHINWARI, M. W.; DEEN, M. J.; STARIKOV, E. B.; CUNIBERTI, G. Electrical conductance in biological molecules. **Advanced Functional Materials**, [*s.l*], v. 20, n. 12, p. 1865–1883, 2010.

SOUSA, J. S. de; FREIRE, R. S.; SOUSA, F. D.; RADMACHER, M.; SILVA, A. F. B.; RAMOS, M. V.; MONTEIRO-MOREIRA, A. C. O.; MESQUITA, F. P.; MORAES, M. E. A.; MONTENEGRO, R. C.; OLIVEIRA, C. L. N. Double power-law viscoelastic relaxation of living cells encodes motility trends. **Scientific Reports**, [*s.l*], v. 10, n. 1, p. 4749, mar. 2020.

SURESH, S. Biomechanics and biophysics of cancer cells. **Acta Biomater.**, [*s.l*], v. 3, n. 4, p. 413–438, jul. 2007.

TAKASHIMA, S. Membrane capacity of squid giant axon during hyper- and depolarizations. **The Journal of Membrane Biology**, [*s.l*], v. 27, n. 1, p. 21–39, Dec 1976. ISSN 1432-1424. doi:10.1007/BF01869127.

TRIYONO, D.; FITRIA, S. N.; HANIFAH, U. Dielectric analysis and electrical conduction mechanism of la1-x bi x FeO3 ceramics. **RSC Adv.**, [*s.l*], v. 10, n. 31, p. 18323–18338, may 2020.

TSAI, C.-C.; HUNG, H.-H.; LIU, C.-P.; CHEN, Y.-T.; PAN, C.-Y. Changes in plasma membrane surface potential of pc12 cells as measured by kelvin probe force microscopy. **PLOS ONE**, [*s.l*], v. 7, n. 4, p. 1–7, 04 2012. doi:10.1371/journal.pone.0033849.

TSAI, S.-L.; WANG, M.-H.; CHEN, M.-K.; JANG, L.-S. Analytical and numerical modeling methods for electrochemical impedance analysis of single cells on coplanar electrodes. **Electroanalysis**, [*s.l*], v. 26, n. 2, p. 389–398, 2014. doi:10.1002/elan.201300544.

WILSON, J. R.; CLARK, R. B.; BANDERALI., U.; GILES, W. R. Measurement of the membrane potential in small cells using patch clamp methods. **Channels**, Taylor Francis, [*s.l*], v. 5, n. 6, p. 530–537, 2011. doi:10.4161/chan.5.6.17484.

WU, F.; ZHOU, B.; WANG, J.; ZHONG, M.; DAS, A.; WATKINSON, M.; HING, K.; ZHANG, D.-W.; KRAUSE, S. Photoelectrochemical imaging system for the mapping of cell surface charges. **Analytical Chemistry**, [*s.l*], v. 91, n. 9, p. 5896–5903, 2019. doi:10.1021/acs.analchem.9b00304.

XU, Y.; XIE, X.; DUAN, Y.; WANG, L.; CHENG, Z.; CHENG, J. A review of impedance measurements of whole cells. **Biosens. Bioelectron.**, [*s.l*], v. 77, p. 824–836, mar. 2016.

YAN, H.; WU, H. Patch clamp measurements on-chip. *In*: LI, D. (ed.). **Encyclopedia of Microfluidics and Nanofluidics**. Boston, MA: Springer US, 2013. p. 1–13. ISBN 978-3-642-27758-0.

ZHAO, L.; DU, X.; FANG, B.; LIU, Q.; YANG, H.; LI, F.; SHENG, Y.; ZENG, X.; ZHONG, H.; ZHAO, W. Direct investigations of the electrical conductivity of normal and cancer breast cells by conductive atomic force microscopy. **Ultramicroscopy**, [*s.l*], v. 237, p. 113531, 2022. ISSN 0304-3991. doi:10.1016/j.ultramic.2022.113531.

ZHAO, W.; CHEONG, L.-Z.; XU, S.; CUI, W.; SONG, S.; ROURK, C.; SHEN, C. Direct investigation of current transport in cells by conductive atomic force microscopy. **Journal of Microscopy**, [*s.l*], v. 277, n. 1, p. 49–57, 2020. doi:10.1111/jmi.12861.

ZHAO, W.; CUI, W.; XU, S.; WANG, Y.; ZHANG, K.; WANG, D.; CHEONG, L.-Z.; BESENBACHER, F.; SHEN, C. Direct investigation of charge transfer in neurons by electrostatic force microscopy. **Ultramicroscopy**, [*s.l*], v. 196, p. 24–32, 2019. ISSN 0304-3991. doi:10.1016/j.ultramic.2018.09.015.

ZHOU, G.; DUAN, S.; LI, P.; SUN, B.; WU, B.; YAO, Y.; YANG, X.; HAN, J.; WU, J.; WANG, G.; LIAO, L.; LIN, C.; HU, W.; XU, C.; LIU, D.; CHEN, T.; CHEN, L.; ZHOU, A.; SONG, Q. Coexistence of negative differential resistance and resistive switching memory at room temperature in TiO_xmodulated by moisture. **Adv. Electron. Mater.**, [*s.l*], v. 4, n. 4, p. 1700567, apr. 2018.

ZHU, S.; SUN, B.; RANJAN, S.; ZHU, X.; ZHOU, G.; ZHAO, H.; MAO, S.; WANG, H.; ZHAO, Y.; FU, G. Mechanism analysis of a flexible organic memristive memory with capacitance effect and negative differential resistance state. **APL Mater.**, [*s.l*], v. 7, n. 8, p. 081117, aug. 2019.